Optimizing observation strategies for redshifted HI detection using upgraded Ooty Radio Telescope (ORT)

Bharat Kumar Gehlot

A dissertation submitted for the partial fulfilment of BS-MS dual degree in Science

Indian Institute of Science Education and Research Mohali
April 2014

Certificate of Examination

This is to certify that the dissertation titled **"Optimizing observation strategies for redshifted HI detection using upgraded Ooty Radio Telescope (ORT)"** submitted by **Bharat Kumar Gehlot** (Reg. No. MS09036) for the partial fulfillment of BS-MS dual degree programme of the Institute, has been examined by the thesis committee duly appointed by the Institute. The committee finds the work done by the candidate satisfactory and recommends that the report be accepted.

Dr. Rajeev Kapri   Dr. Harvinder Kaur Jassal   Dr. Jasjeet Singh Bagla
                                                                                                (Supervisor)

Dated: April 25, 2014

Declaration

The work presented in this dissertation has been carried out by me under the guidance of Dr. Jasjeet Singh Bagla at the Indian Institute of Science Education and Research Mohali.

This work has not been submitted in part or in full for a degree, a diploma, or a fellowship to any other university or institute. Whenever contributions of others are involved, every effort is made to indicate this clearly, with due acknowledgement of collaborative research and discussions. This thesis is a bonafide record of original work done by me and all sources listed within have been detailed in the bibliography.

Bharat Kumar Gehlot

(Candidate)

Dated: April 25, 2014

In my capacity as the supervisor of the candidate's project work, I certify that the above statements by the candidate are true to the best of my knowledge.

Dr. Jasjeet Singh Bagla

(Supervisor)

Acknowledgments

This thesis would not have been possible without the active help and immense support of a gamut of people. Firstly, I am deeply indebted to Prof. Jasjeet Singh Bagla, my thesis advisor. His zeal for excellence, dedication towards astronomy and astrophysics, overall enthusiasm and a positive attitude is what attracted me to work with him. I have learnt a lot from him, he has fearlessly exposed me to a wide variety of problems, without letting me lose my self-confidence when things wouldn't work, and come up with life-saving ideas just when I would be giving up hope. It has been a pleasure to work with him and I wish him all the good health and happiness that he deserves.

I would like to thank Prof. Somnath Bharadwaj and Sk. Saiyad Ali for their support and helpful discussions over the internet and personally when I was stuck at some point. My special thanks to Prof. Jayaram Chegalur who allowed me to work with him during summers in 2012 and our discussions on the various aspects of interferometry. I would like to thank Viswesh for his help and fruitful discussions on the software part of ORT which helped me to gain sufficient knowledge to write a chapter on ORT upgrade in my thesis. I also thank Dr. P. K. Manoharan for his help in understanding the hardware backend of ORT. Thanks to Kanan K Datta for our discussions on noise calculations during ASI meet and queries over the phone at the time when I needed it most. I also thank Prof. C. R. Subhramanya for his reviews on my work and various ideas which helped me to improve my work.

Many thanks to my friends at IISER Mohali, including Jugal Pant who was always there with me during fun and misery, Prateek and Nishant Malik for good fun and enjoyment, Deep Raj who was always there to listen my yabbering and all the others who made my stay at IISER mohali lively and joyful. I would like to especially thank Prasun Dutta, for our trekking trips, discussions and his help whenever I had some technical problem.

Last, but not the least, I wish to thank my family. In fact, I cannot begin to express my gratitude towards my family, and especially my parents, for all the moral and practical support they have provided selflessly, and for many, many years. They allowed me to pursue my dreams, without putting any kind of pressure. It is only because of their efforts that I didn't just give up and run away! Daddy, for being a constant source of inspiration, knowledge since I was a kid and encouragement. Mummy, for her loving and affectionate nature.

I express my deepest appreciation to all faculty members, library staff and administrative staff of IISER Mohali.

Contents

List of Figures

Abstract

Observations of the high-redshift Universe with the 21 cm hyperfine line of neutral hydrogen promise to open an entirely new window onto the early phases of the cosmic structure formation. The study of the HI 21 cm power spectrum provide a promising tool to map large scale HI distribution in post-reionization era ($z \leq 6$). The majority of the recent or upcoming radio interferometric experiments are aimed at measuring the HI 21 cm signal statistically and map out the large scale HI distribution at high redshifts. Ooty Radio telescope (ORT) is currently being upgraded, after the planned upgrade it may be used as an interferometer. The upgraded ORT can detect signal at frequency $\nu = 326.5$ MHz which corresponds to an HI signal at redshift $z = 3.35$. In the thesis, we develop visibility correlations formalism for upgraded ORT, power spectrum for redshifted HI signal is measured using N-body simulations[2]. We will investigate different observation strategies using the telescope for statistical detection of HI signal above good noise level within optimized integration time and suitable number of beams.

Chapter 1

Introduction

The study of formation and evolution of the cosmic structure has been an important subject in cosmology. The complex objects that surround us today grew out of the remarkably smooth medium that emerged from the Big Bang. The tiny density fluctuations in this smooth universe grew via gravitational instability and finally formed a cosmic web of sheets and filaments.

This hypothesis has been successful in explaining observations of both the early Universe and local structures. But two significant gaps remain in the story: the cosmic "dark ages" between the last scattering surface of the CMB & the formation of the first luminous structures and the era of "first light" that stretches from the formation of these sources to the full reionization of the intergalactic medium (IGM). Observations from these epochs can offer us to study the transition between the linear and nonlinear regimes of gravitational growth, the characteristics of the first stars and quasars, and their influence on the Universe around them. They provide an opportunity to connect our detailed pictures of the early Universe with the galaxies around us.

Observations of the high-redshift Universe with the 21 cm hyperfine line of neutral Hydrogen promise to open an entirely new window onto the early phases of the cosmic structure formation. Observations of redshifted 21 cm radiation can in principle be carried out over a large redshift range starting from the cosmological Dark Ages through the Epoch of Reionization to the present epoch [7][18], allowing us to study both the evolution history of neutral Hydrogen as well as the growth of structures in the universe [18][2][41]. Redshifted 21 cm observations also hold the potential of allowing us to probe the expansion history of the Universe [11][38].

In the following chapters we describe the upgradation of Ooty Radio telescope(ORT). ORT is being upgraded from analog to digital backend in nearly two independent

phases viz. phase **I** & **II** after which the telescope may be used as an interferometer. We also describe the visibility formalism for the corresponding phases and use this formalism to quantify angular and frequency domain fluctuations of background radiation using multi-frequency angular power spectrum $C_l(\Delta\nu)$. Finally, we discuss the prospects of HI detection with upgraded ORT.

1.1 Evolution of cosmic structure

The exceedingly complex objects that surround us today are believed to have grew out of the remarkably simple and smooth universe that emerged from the Big Bang. The tiny density fluctuations that we observe in the cosmic microwave background (CMB) grew through gravitational instability until they collapsed into the "cosmic web" of sheets, filaments, and halos. The main goal of study of formation of large scale structures is to understand the formation and physical properties of galaxies and their clustering starting from given initial perturbations with a given spectrum. On large scales the clustering properties are dictated by gravity alone. However on small scales non- gravitational effects contribute significantly.

In standard big-bang cosmology[26][39], the assumption of homogeneity and isotropy of Universe on large scales requires the Friedmann-Lemaitre-Robertson-Walker (FLRW) metric,

$$ds^2 = -c^2dt^2 + a^2(t)\left[\frac{dx^2}{1-kx^2} + x^2(d\theta^2 + \sin^2\theta d\phi^2)\right] \qquad (1.1)$$

Here $a(t)$ is the scale factor, (x, θ, ϕ) are the comoving coordinates and k is the curvature constant. k can three values i.e. +1, 0 or -1 corresponding to which Universe can be closed, flat or open respectively. t is the cosmic time.

The comoving coordinates (x) are different from the observationally measured coordinates, also known as physical coordinates (r). These two are related as, $\mathbf{r}(t) = a(t)\mathbf{x}$. Therefore, proper velocity of a particular object is given by

$$\dot{\mathbf{r}}(t) = \dot{a}(t)\mathbf{x} + a(t)\dot{\mathbf{x}} = \mathbf{v}_h + \mathbf{v}_p \qquad (1.2)$$

Where $\mathbf{v}_p$ is called peculiar velocity of objects. In absence of peculiar velocities, we can write above relation as:

$$\mathbf{v}_h = \left[\frac{\dot{a}(t)}{a(t)}\right]a(t)\mathbf{x} = \left[\frac{\dot{a}(t)}{a(t)}\right]\mathbf{r}(t) \equiv H(t)\mathbf{r}(t) \qquad (1.3)$$

This is known as Hubble Law with $H(t)$ being Hubble's parameter. At present time, i.e., at $t = t_0$, $H(t) = H_0 = 71.9^{+2.6}_{-2.7}$ Km/s/Mpc [20][25]. For FLRW metric, Einstein's field equations can be solved to give

$$\frac{\dot{a} + k^2}{a^2} = \frac{8\pi G}{3}\bar{\rho} + \frac{\Lambda}{3} \quad \text{and,} \tag{1.4}$$

$$2\frac{\ddot{a}}{a} + \frac{\dot{a} + k^2}{a^2} = -8\pi G p + \Lambda \tag{1.5}$$

Where Λ is the cosmological constant, G is the gravitational constant, p is the pressure and $\bar{\rho}$ is the energy density. These two equations alongwith the equation of state $p = p(\bar{\rho})$, completely determine the three functions, $a(t)$, $\rho(t)$, & $p(t)$.

The constituents in our Universe can be classified as radiation and relativistic matter with energy density $\bar{\rho}_{rad}$, non-relativistic matter with energy density $\bar{\rho}_{nr}$, and dark energy cosmological constant $\bar{\rho}_\Lambda$. The total energy density is the sum of all the components, i.e. $\bar{\rho} = \bar{\rho}_{rad} + \bar{\rho}_{nr}$.

It is possible to define critical density ρ_c in terms of the Hubble constant,

$$\rho_c = \frac{3H_0^2}{8\pi G} \tag{1.6}$$

Dimensionless density parameter Ω_i can also be defined for i^{th} component of matter, i.e.

$$\Omega_i \equiv \frac{\bar{\rho}_i}{\rho_c} \tag{1.7}$$

Eq.1.4 can be modified to get the following form,

$$\frac{\dot{a} + k^2}{a^2} = H_0^2 \left[\Omega_{rad} \left(\frac{a_0}{a}\right)^4 + \Omega_{nr} \left(\frac{a_0}{a}\right)^3 + \Omega_\Lambda \right] \tag{1.8}$$

$$H^2(a) = H_0^2 \left[\Omega_{rad} \left(\frac{a_0}{a}\right)^4 + \Omega_{nr} \left(\frac{a_0}{a}\right)^3 - \Omega_k \left(\frac{a_0}{a}\right)^2 + \Omega_\Lambda \right] \tag{1.9}$$

Where $\Omega_k = \Omega_{rad} + \Omega_{nr} + \Omega_\Lambda - 1$, is the density parameter due to curvature with $k = a_0^2 H_0^2 \Omega_k$ and $\Omega_\Lambda = \frac{\Lambda}{3H_0^2}$. According to observations, $\Omega_k = \Omega_{tot} - 1 \approx 0$ [20], this means that universe is nearly flat .

3

1.2   Redshifted HI detection

Galaxies are believed to form when gas in highly over-dense haloes cools and collapses to form stars in significant numbers [12][28]. The formation of first stars in turn leads to emission of UV radiation that starts to ionize the inter-galactic medium (IGM) [24][44]. The period of transition of the IGM from a completely neutral to a completely ionized state is known as the epoch of reionization (EoR). Observations indicate that the process of reionization was completed before $z \sim 6$ [4][17]. Prior to the EoR, almost all the Hydrogen in the universe is in atomic form. Through the EoR Hydrogen is ionized till we are left with almost no HI in the inter-galactic medium and almost all the HI resides in the inter stellar medium (ISM) of galaxies.

In the post reionization era ($z < 6$) much of the inter-galactic medium (IGM) is highly ionized and does not contain a significant amount of neutral Hydrogen. Most of the neutral Hydrogen resides in relatively rare damped Lyman-α systems (DLAS) [40]. These systems which are seen as Damped Lyman-α absorption lines (DLAs) in quasar spectra are known to contain the bulk of the HI. The observations of DLAs indicate that at redshifts $1 \leq z \leq 6$, the neutral hydrogen content of the universe is almost constant with a density parameter $\Omega_{HI} \sim 0.001^*$. At low redshifts, HI content can be estimated directly through emission in hyperfine transition. The collective emission from the undetected regions is present as a very faint background in all radio observations at frequencies below 1420 MHz. The fluctuations in this background radiation carry an imprint of the HI distribution at the redshift z where the radiation originated. The possibility of observing the HI emission from the post-reionization era, holds the potential of providing us with a new observational probe of large-scale structures [3][9][10][41].

It has been proposed that the Baryon Acoustic Oscillation (BAO) in the redshifted 21 cm signal from the post-reionization era $z \leq 6$ is a very sensitive probe of dark energy [13][42]. The BAO peak wavelengths can be used as a cosmological standard ruler: observation of the angular size of the peak wavelengths across a range of red-shifts allows accurate measurement of the expansion history. The oscillations also produced density structure in the atomic gas and dark matter which is still detectable today [13]. By scanning across frequency, 21 cm observations will probe the HI distribution at different times in cosmic history which will allow us to construct 21 cm

---

$^*\Omega_{HI} \equiv \dfrac{\rho_{HI}(z)}{\rho_c(z=0)}$

tomography of the IGM. A compact interferometers with wide field of view are needed to cover the BAO length-scale.

Realizing this great potential, the majority of the recent or upcoming radio-interferometric experiments such as LOFAR, MWA, SKA, PAPER etc. are aimed at measuring the HI 21 cm signal statistically and map out the large scale HI distribution at high redshifts. Ooty Radio telescope is currently being upgraded, after the planned upgrade it may be used as an interferometer and will have multibeaming feature. The upgradation will lead to improved sensitivity and an increased field of view. The ORT holds the potential of measuring the $z = 3.35$ power spectrum, opening the possibility of probing large-scale structure formation at an hitherto unexplored redshift. ORT can also probe the BAO length scale.

1.3 Ooty Radio Telescope

The Ooty Radio Telescope is one of the largest telescopes in the world, operating at 326.5 MHz. It is an equatorially mounted, off-axis parabloic reflector type phased array of 1056 dipoles. It is a parabolic cylindrical antenna which is 530 m long in north-south direction and 30 m wide in east-west direction.

The legacy system is a phased array of 1056 dipoles. The E-W tracking is done by rotation of the cylindrical reflector along its axis and N-S tracking is done by electronically phasing the array. The feed system consists of 22 modules with each module serving 48 dioples. The signal from each module is carried over to receiver room via 30MHz Intermediate Frequency (IF) line. The legacy system is able to produce 12 phase switched beams and 12 total power beams separately.

The array is currently being upgraed to improve sensitivity and the Field of View (FoV). After the upgradation, it may be used as an interferometer and will have multibeaming feature. ORT is being upgraded in two nearly independent stages, Phase **I** and Phase **II**.

Phase **I** consists of 40 antenna elements where each element is the combination of 24 dipoles. The signal from these antenna elements is amplified, conditioned and directly digitized in the field and sent to the receiver room over 4 full duplex fibre optic links. The receiver system consists of pooler/bridge systems to pool this data from the four fibre optic links from the field. The data is collected in distributed manner using two server class machines. In Phase **I**, Each antenna element is 11.5m along the length of the cylinder and 30m wide. The smallest baseline corresponds to

Figure 1.3.1: The Ooty Radio Telescope.

antenna separation of 11.5m and longest baseline corresponds to 448.5m. The system has frequency bandwidth of 18 MHz.

Phase **II** consists of 264 antenna elements where each antenna is the combination of 4 dipoles. The signal from these antenna elements is amplified, conditioned and directly digitized in the field and sent over to the receiver room over 44 fibre optic links which are connected to the pooler/bridge systems, which produce the final output in 8 independent sets of 11 GigE links. These 88 Gigabit ethernet links are connected to a unmanaged set of ethernet switches which are to be linked to a High Performance Cluster (HPC). Currently HPC used is a set of many-core processors with Intel's Sandy Bridge architecture. Each node will receive data from the bridge subsystem through a set of 11 GigE links. Each node have a quad 8-core processor board with Intel Xeon Phi coprocessor. In Phase **II**, each antenna element is 1.9 m along the length of the cylinder and 30 m wide. The smallest baseline corresponds to the antenna separation of 1.9 m and longest baseline corresponds to 505.0 m. The system has frequency bandwidth of 30 MHz.

We discuss about the Ooty Radio Telescope's design and structure, visbility correlation formalism, and possibility of HI detection with the upgraded system in following chapters.

6

Chapter 2

Ooty Radio Telescope

The Ooty Radio Telescope is one of the largest telescopes in the world, operating at 327 MHz. It consists of a parabolic cylindrical antenna which is 530 m long in north-south direction and 30 m wide in east-west direction. It is an equatorially mounted phased array of 1056 dipoles placed along the focal line of the reflector. The East-West steering (R.A) is done by the mechanical rotation of the telescope about its N-S axis and steering of beam in north-south direction(Declination) is achieved by introducing appropriate delays between the dipoles.

2.1   Antenna Design and Structure

ORT consists of an asymmetric parabolic cylindrical antenna which is 530 m long in north-south and 30 m wide in east-west direction. The long axis of the telescope is alinged along north-south direction on a hill whose slope is 11° which is equal to the latitude of the observatory which makes its long axis parallel to earth's rotation axis and provides a natural equatorial mounting(see fig.2.1.1) to the telescope. The reflector is an offset type parabolic reflector, i.e. the feed is located at the focal point of the reflector, but the reflector is an asymmetric segment of a parabola, so the focus is offset to the side of the reflector (see fig. 2.1.2). Thus the feed does not obstruct the field of view.

The parabolic cylinder consists of 24 parabolic frames, each 30 m wide, supported on 12 to 18 m high towers. The parabolic frames have a focal length **a** of 16.5 m and are spaced 23 m apart along the north-south baseline of 530 m. The reflecting surface is made up of 1100 stainless steel wires running parallel to the axis of the cylinder.
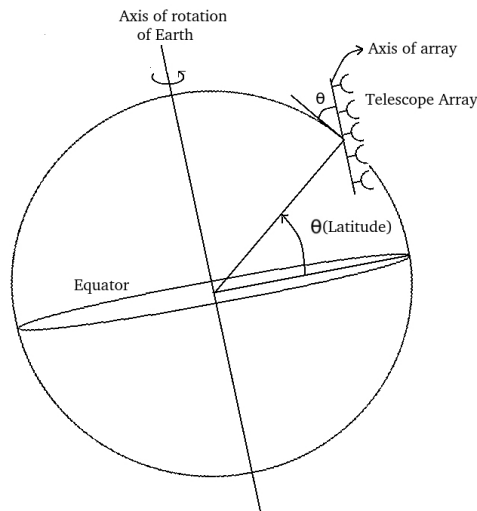
Figure 2.1.1: An equatorially mounted array.
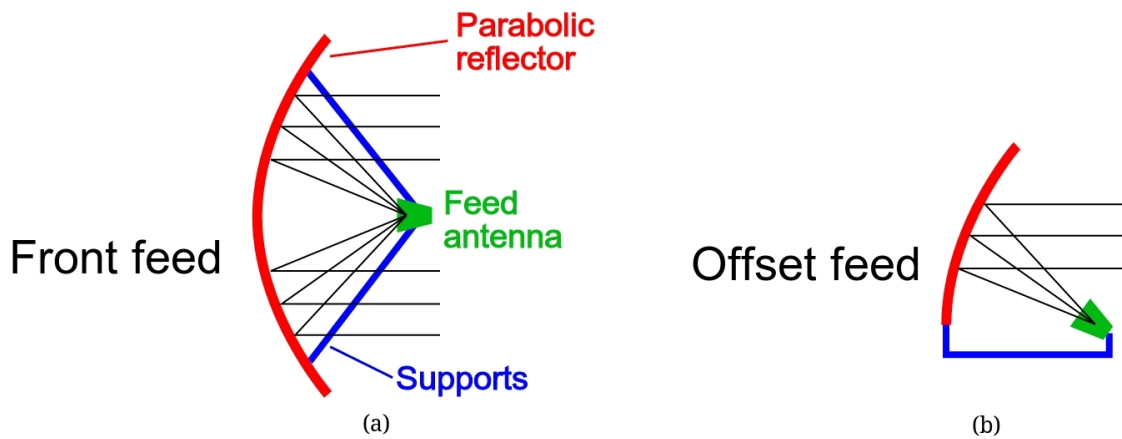
Figure 2.1.2: (a) Front feed type antenna (b) Offset feed type antenna.

The wires have a projected spacing of 20 mm in the central portion, 25 mm midway and 40 mm at the edges of the parabolic surface. The parabolic reflector is illuminated by a linear and uniform array of 1056 half wavelength dipoles placed along the focal line at the phase center of a 90° corner reflector. The 24 frames are rotated in unison through a common driveshaft. Equatorial mount provides a Coverage of hour angle from 04h 05 min east to 05h 30 min west. ORT is able to track a celestial object for about 9.5 hours continuously by mechanical rotation of the telescope. Figure 2.1.3(a) represents the geometry of the antenna system and figure 2.1.3(b) shows the sketch of one of the 24 parabolic frames of ORT.

The array is currently being upgraded after which it may be used as a radio interferometer. The planned upgradation will lead to improved sensitivity, Field of
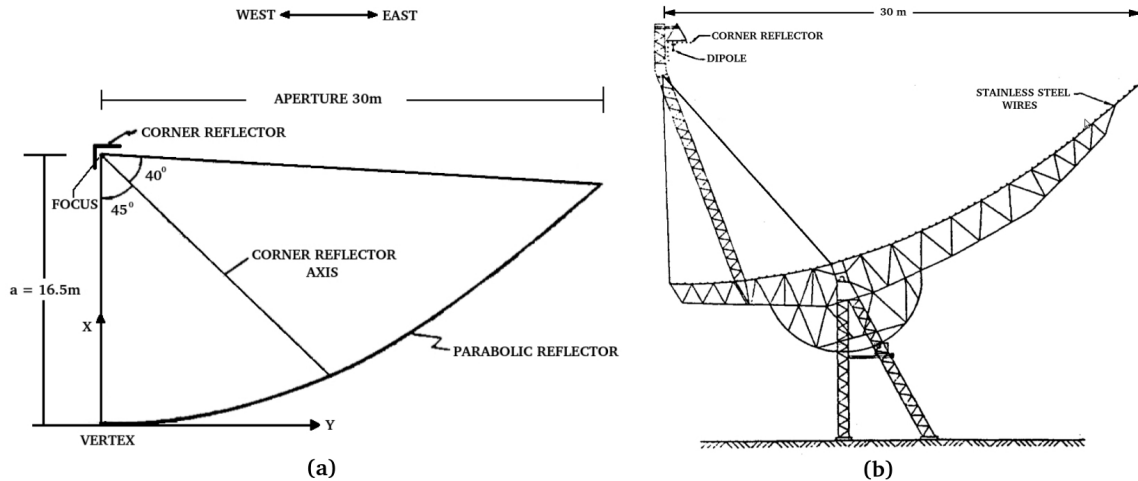
Figure 2.1.3: (a) Geometry of the antenna system. (b) Sketch showing one of the 24 parabolic frames of ORT.[19][35]

View and will have multibeaming feature. We discuss about the basic physics behind the phasing of arrays and radio interferometry, the electronics and system design of the legacy system and the current upgradation in detail in following sections.

2.2   Theory of Linear Arrays

Use of antenna arrays is one way of increasing the effective resolution and collecting area of a radio telescope. An array usually consists of several discrete antenna elements arranged in a particular configuration. Most often this configuration produces an unfilled aperture antenna, where only part of the overall aperture is filled by the antenna structure.

The outputs (voltage signals) from the array elements can be combined in various ways to achieve different results. If the outputs are multiplied in distinct pairs in a correlator and processed further to make an image of the sky brightness distribution, the array is referred to as an interferometer. If the outputs are combined, with appropriate phase shifts, to obtain a single, total power signal from the array – such an array is generally referred to as a phased array. In this section, we will primarily be concerned with the study of phased arrays.

2.2.1 Antenna Patterns

The most important characteristic of an antenna is its ability to absorb radio waves incident upon it. This is usually described in terms of its effective aperture. The effective aperture of an antenna is defined as

$$A_e = \frac{\text{Power density available at the antenna terminals}}{\text{Flux density of the wave incident on the antenna}} \quad \text{m}^2$$

The effective area is a function of the direction of the incident wave, because the antenna works better in some directions than in others. Hence

$$A_e = A_e(\theta, \phi)$$

This directional property of the antenna is often described in the form of a power pattern. The power pattern is simply the effective area normalized to be unity at the maximum, i.e.

$$f(\theta, \phi) = \frac{A_e(\theta, \phi)}{A_e^{max}} \tag{2.1}$$

Field pattern is also used to specify the directional property of an antenna. Consider an antenna receiving radio waves from a distant point source. The voltage at the terminals of the antenna as a function of the direction to the point source, normalized to unity at maximum, is called the field pattern $f(\theta, \phi)$ of the antenna.

The pattern of an antenna is the same regardless of whether it is used as a transmitting antenna or as a receiving antenna, i.e. if it transmits efficiently in some direction, it will also receive efficiently in that direction. This is called Reciprocity, and follows from Maxwell's equations. From reciprocity it follows that the electric field far from a transmitting antenna, normalized to unity at maximum, is simply the Field pattern $f(\theta, \phi)$. Since the power flow is proportional to the square of the electric field, the power pattern is the square of the field pattern.

A typical power pattern is shown in Figure 2.2.1. The power pattern has a primary maximum, called the main lobe and several subsidiary maxima, called side lobes. The points at which the main lobe falls to half its central value are called the Half Power points and the angular distance between these points is called the Half Power Beamwidth (HPBW). The minima of the power pattern are called nulls. For radio astronomical applications one generally wants the HPBW to be small (so that sources close to each other on the sky are not confused with one another), and the sidelobes
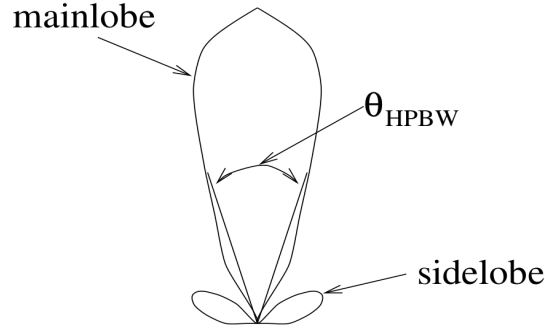
Figure 2.2.1: A typical power pattern of an antenna.

to be low (to minimize stray radiation). From diffraction theory it can be shown that the HPBW of a reflecting telescope is given by

$$\Theta_{HPBW} \sim \frac{\lambda}{D}$$

where D is the physical dimension of the antenna.

2.2.2 Array of 2 elements

Consider two isotropic (sources which radiate the same intensity in all directions and has no preferred direction of radiation) point sources separated by a distance d, as shown in figure 2.2.2. The net far field in direction θ is given by

$$E(\theta) = E_1 \ e^{j\psi/2} + E_2 \ e^{-j\psi/2} \tag{2.2}$$

Where $\psi = kd\sin\theta + \delta, k = 2\pi/\lambda$ and δ is the intrinsic phase difference between the two sources. E_1 and E_2 are the amplitudes of the electric field due to the two sources, at the distant point. The reference point for the phase, referred to as the phase centre, is taken halfway between the two elements.

If the two sources have equal strength, $E_1 = E_2 = E_0$, eq. 2.2 becomes

$$E(\theta) = 2E_0 \ \cos(\psi/2) \tag{2.3}$$

The power pattern is obtained by squaring the field pattern. By virtue of the reciprocity, $E(\theta)$ also represents the voltage reception pattern obtained when the signals from the two antenna elements are added, after introducing the phase shift δ between them.
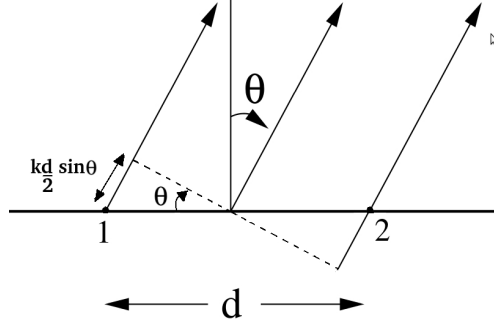
Figure 2.2.2: Geometry of a 2 element array.

For $\delta = 0$ and $d \gg \lambda$, the field pattern of this array shows sinusoidal oscillations for small variations of θ around zero. Non-zero values of δ simply shift the phase of these oscillations by the appropriate value.

If the individual elements are not isotropic but have identical directional patterns, eq. 2.3 is modified by replacing E_0 with the element pattern, $E_i(\theta)$. The final pattern is given by the product of the individual element pattern ($E_i(\theta)$) and the array pattern but with individual elements replaced by the isotropic point sources having the same relative amplitude and phase. The total phase pattern is the sum of the phase patterns of the individual elements and the array of isotropic point sources.

2.2.3 Linear array of n elements of equal Amplitude:

Consider the case of a uniform linear array of n elements (isotropic) of equal amplitude and spacing, as shown in figure 2.2.3. Taking the first element as the phase reference, the far field pattern is given by

$$E(\theta) = E_0(1 + e^{j\psi} + e^{2j\psi} + ... + e^{j(n-1)\psi}) \qquad (2.4)$$

Where $\psi = kdsin\theta + \delta, k = 2\pi/\lambda$ and δ is the progressive phase difference between the sources.

Eq. 2.4 can be rewritten as

$$E(\theta) = E_0 \frac{(e^{nj\psi} - 1)}{(e^{j\psi} - 1)} = E_0 \frac{\sin(n\psi/2)}{\sin(\psi/2)} e^{j(n-1)\psi/2} \qquad (2.5)$$

If the centre of the array is chosen as the phase reference point, then the above result does not contain the phase term of $(n-1)\psi/2$. For nonisotropic but similar
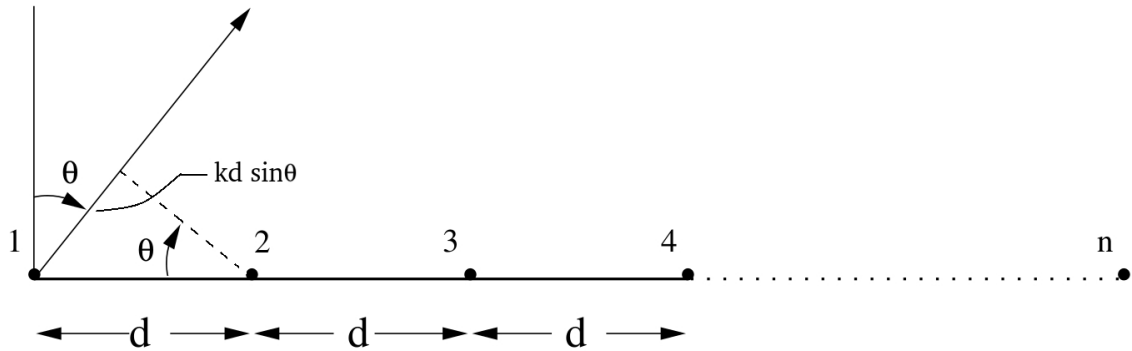
Figure 2.2.3: Geometry of an n element array.

elements, E_0 is replaced by the element pattern $E_i(\theta)$, to obtain the total field pattern (see Fig.2.2.4).

The field pattern in eq. 2.5 has a maximum value of nE_0 when $\psi = 0, 2\pi, 4\pi, ...$ The maxima at $\psi = 0$ is called the main lobe, while the other maxima are called grating lobes. For $d < \lambda$, only the main lobe maxima maps to the physically allowed range of $0 \leq \theta \leq 2\pi$.

The presence of grating lobes in the response of an array is usually an unwanted feature, and it is desirable to reduce their levels as much as possible. For non-isotropic elements, the taper in the element pattern provides a natural reduction of the amplitude of the higher grating lobes. This is illustrated in Figure 2.2.4.
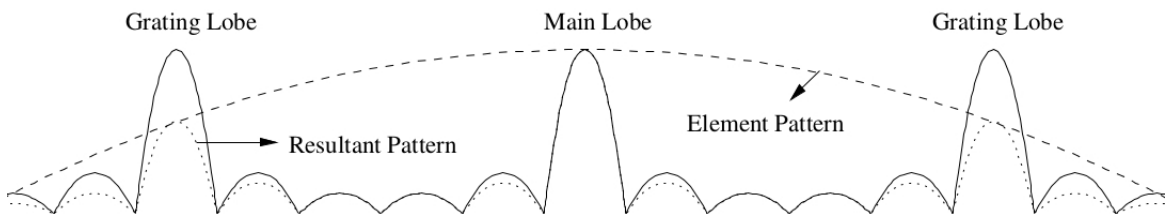
Figure 2.2.4: Array pattern of an array of n identical elements. The solid line is the array pattern. The broad, dashed line curve is element pattern. The resultant of these two is shown as the dotted pattern[14].

By suitable choice of the value of δ, this main lobe maxima can be steered to different values of θ, using the relation $kd\sin\theta = -\delta$. When all the elements of the array are in phase ($\delta = 0$), the maximum occurs at $\theta = 0$, this is referred to as a "broadside" array. For a maximum along the axis of the array ($\theta = 90°$), $\delta = -kd$ is required, giving rise to an "end-fire" array.

The broadside array produces a disc or fan shaped beam that covers a full 360° in the plane normal to the axis of the array. The end-fire array produces a cigar shaped beam which has the same shape in all planes containing the axis of the array.

For the case of $d > \lambda$, the grating lobes are uniformly spaced in $sin\theta$ with an interval of λ/d between adjacent maxima, on θ axis this interval translates to $\leq \lambda/d$.

The uniform, linear array has nulls in the radiation pattern which are given by the condition $\psi = \pm 2\pi l/n, l = 1, 2, 3...$, using this result in $\psi = kd\sin\theta + \delta$ which yields

$$\theta = \sin^{-1}\left[\frac{1}{kd}\left(\pm\frac{2\pi l}{n} - \delta\right)\right] \tag{2.6}$$

For a broadside array ($\delta = 0$),

$$\theta = \sin^{-1}\left(\pm\frac{2\pi l}{nkd}\right) \tag{2.7}$$

Further, if array is long, i.e. $nd \gg l\lambda$, the above relation becomes

$$\theta \simeq \pm\frac{l\lambda}{nd} \simeq \frac{1}{L_\lambda}, \tag{2.8}$$

where L_λ is the length of array in wavelengths and $L_\lambda = (n-1)d/\lambda \simeq nd/\lambda$ for large n. First nulls in array pattern occur at $l = \pm 1$, therefore Beam Width between First Nulls (BWFN) and Half Power Beam Width (HPBW) for such an array is given by

$$\text{BWFN} = \frac{2}{L_\lambda}rad = \frac{114.6^o}{L_\lambda} \text{ and HPBW} = \frac{\text{BWFN}}{2} = \frac{57.3^o}{L_\lambda} \tag{2.9}$$

ORT has HPBW of 5.5 arc min in declination and about 2° in Right Acsension.

2.3   Signals and Noise

2.3.1   Signals

At radio frequencies, strengths of cosmic sources are usually measured in **Jansky (Jy)** named after the famous radio astronomer Karl G. Jansky. For a plane wave from a distant point source falling on the Earth,

$$1\text{Jy} = 10^{-26} \ W/m^2/Hz,$$

I.e., if the energy per unit frequency passing through an area of 1 m^2 held perpendicular to the line of sight to the source is 10^{-26} watts then the source is said to have a brightness of 1 Jy. For an extended source, sky brightness B is the energy flow at Earth per unit area, per unit time, per unit solid angle, per unit Frequency, i.e. the units of brightness are $W/m^2/Hz/sr$.

The sky brightness is also measured in temperature units. Consider a black body at temperature T, the radiation from the black body is described by the Planck spectrum

$$B(\nu) = \frac{2h\nu^3}{c^2} \frac{1}{e^{h\nu/k_BT} - 1} \quad W/m^2/Hz/sr \qquad (2.10)$$

For radio frequencies (~ 1 GHz), $h\nu/k << 1$, hence

$$e^{h\nu/k_BT} \sim 1 + \frac{h\nu}{k_BT}$$

This approximation is known as Rayleigh-Jeans Approximation and is valid through most of radio regime. Applying this approximation to Eq.2.10 we get,

$$B(\nu) \simeq \frac{2\nu^2}{c^2} k_BT = \frac{2k_BT}{\lambda^2} \qquad (2.11)$$

Therefore, Brightness temperature T_B can be written as

$$T_B = \frac{\lambda^2}{2k_B} B(\nu) \qquad (2.12)$$

Where $B(\nu)$ is the sky brightness of the source. The brightness temperature of an extended source is also defined by the same relation. In general, brightness temperature T_B has no relation to the physical temperature of the source.

2.3.2   Noise

An antenna absorbs power from the radio waves that fall on it, this power is usually specified in temperature units. In radio regime, the power per unit frequency due to thermal fluctuations is well approximated by the Nyquist formula:

$$P = k_BT$$

In analogy with this, if a power P(per unit frequency) is available at an antenna's terminals the antenna is defined to have an antenna temperature of

$$T_A = \frac{P}{k_B} \qquad (2.13)$$

Note that the antenna temperature does not correspond to the physical temperature of the antenna. Similarly the total power available at a radio telescope terminals, referred to the receiver inputs is defined as the system temperature T_{sys}.

$$T_{sys} = \frac{\text{Total power referred to receiver inputs}}{k_B} \qquad (2.14)$$

The system temperature when looking at blank sky is a measure of the total random noise in the system and hence it is desirable to make the system temperature as low as possible. Noise from the various sub systems that make up the radio telescope are uncorrelated and hence add up linearly. The system temperature can be very generally written as

$$T_{sys} = T_{sky} + T_{spill} + T_{loss} + T_{receiver} \qquad (2.15)$$

T_{sky} is the contribution of the background sky brightness. At all frequencies the sky contributes at least 3K from the cosmic background radiation. The feed antenna also picks up stray radiation from the ground (which radiates approximately like a blackbody at 300 K) around the edge of the reflector. This added noise is called spillover noise(T_{spill}).

Any lossy element in the feed path will also contribute noise (T_{loss}) to the system. This follows from Kirchoff's law which states that good absorbers are also good emitters, and that the ratio of emission to absorption in thermodynamic equilibrium is given by the Planck spectrum at the absorber's physical temperature. The receiver also adds noise to the system, which is characterized by T_{rec}. The noise added after the first few stages of amplification is usually an insignificant fraction of the signal strength and can often be ignored.

2.3.3   Signal to Noise ratio

Since the signals in a radio telescope are random in nature, the output of a total power detector attached to a radio telescope too will show random fluctuations. But given that the signal from a source is also random in nature, it is very difficult to decide

whether the increase in power is due to an astrophysical source or just a random fluctuation. In order to make this decision, rms noise in the fluctuations need to be calculated. Supposing a telescope with system temperature T_{sys}, gain G, and bandwidth $\Delta\nu$, the rms noise after integrating a signal of bandwidth $\Delta\nu$ Hz for τ seconds is $T_{sys}/\sqrt{\Delta\nu\tau}$. The increase in system temperature is just GS, where S is the flux density of the source. The signal to noise ratio is hence

$$\text{snr} = \frac{GS\sqrt{\Delta\nu\tau}}{T_{sys}} \tag{2.16}$$

This equation determines the sensitivity of a radio telescope. For sufficiently large signal to noise ratio, one can be confident of having detected the source.

2.4 Legacy System

The legacy receiver system of ORT can be divided into two parts: Front End and Back End. All the elctronics at the antenna is referred to as Front end and all the electronics in receiver room is referred to as back end.

2.4.1 ORT Front end

ORT front end consists of Antenna system (cylindrical parabolic reflector) and the feed system. The antenna system has already been discussed in section 2.1. The feed system consists of an array of 1056 half wavelength dipoles and 22 modules, each module corresponds to 48 dipoles[31].

ORT Module

In a module, the outputs of 48 dipole antennas are combined to produce a single output. Each dipole in a module is followed by a Low Noise Amplifier (LNA) and a 4-bit phase shifter. A series of power combiners is used to combine the signal from 48 dipoles(after passing through LNA and phase shifters), the combined signal is fed to a RF amplifier(326.5 MHz) and passed to a mixer which downconverts the signal to 30 MHz IF signal. This IF signal is then transmitted to the receiver room[31]. Fig.2.4.1 shows the block diagram of an ORT module.
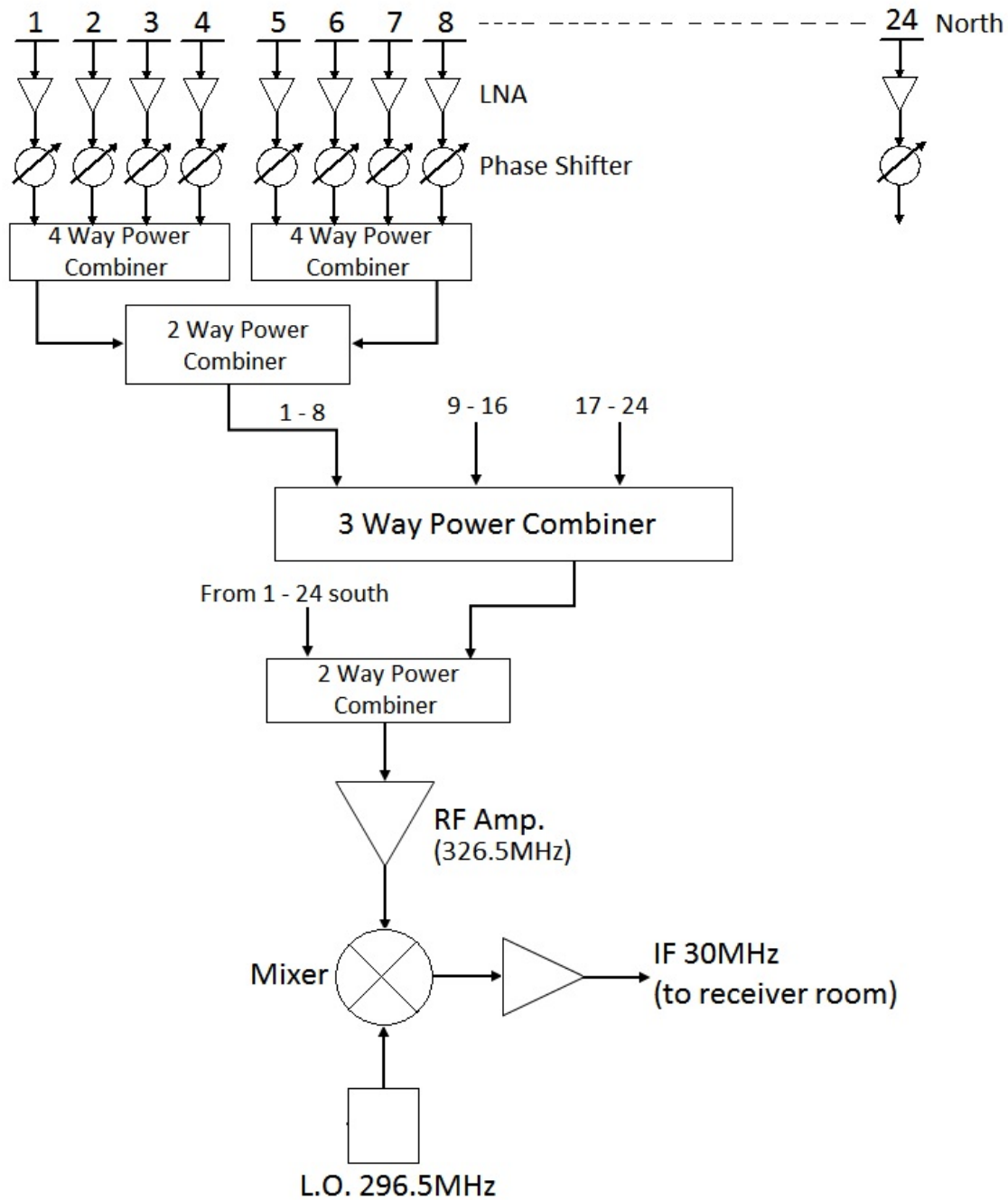
Figure 2.4.1: Block diagram of a Module[31].

Low Noise Amplifier (LNA)

Low Noise Amplifier (LNA) amplifies the signal from a dipole and passes it to the phase shifter. LNA comes immediately after the dipole and plays a major role in determining the system noise temperature, and thus the overall sensitivity of the

telescope. Adding LNA behind each dipole compensates for the loss of signal in the transmission through the phase shifter. It should have the lowest achievable noise figure at the frequency of operation. As all the 1056 LNAs in the array are combined in phase, it is very important that they should be extremely stable (the Gain and noise figure remain almost constant for long operating times) for coherent addition of signals from the 1056 dipoles. The use of LNAs also simplifies the design of RF transmission units. LNAs have gain of 20 dB at 327 MHz and a noise temperature of about 50 K[31].

The Phase Shifter

The basic requirement for phasing an array is to combine the signals from the elements with proper delay and phase adjustments so that the beam can be pointed or steered in the chosen direction. Some of the earliest methods employed techniques for mechanically switching in different lengths of cables between each element and the summing point, to introduce the delays required to phase the array for different directions. The job became somewhat less cumbersome with the use of electronic switches, such as PIN diodes*[31].

Another method of phasing involves the use of phase shifters at each element of the array. This can be achieved by using ferrite devices or by switching microstrip delay lines, using electronic switches. The phase increments are usually implemented in binary steps (for example $\lambda/2, \lambda/4, \lambda/8, ...$). In this scheme, the value of the smallest incremental phase difference controls the accuracy of the phasing that can be achieved.

The dipole array employs 4-bit phase shifters for electronic steering of the telescope beam in N-S direction. The phase shifters consist of microstrip lines of 50Ω characteristic impedance which can be switched using PIN diodes. The phases of the dioples can be shifted by 4 different values i.e. $\lambda/2$, $\lambda/4$, $\lambda/8$ and $\lambda/16$ respectively. The phase shifters for the two halves of each module consisting of 24 dipoles are such that the north half and the south half are complementary[31].

Combining Network

The outputs from the 4 phase shifters are combined using a 4-way power combiner to produce a single output, two such outputs are fed to a 2-way combiner (see fig.2.4.2) to

---

*A diode with a wide, lightly doped 'near' intrinsic semiconductor region between a p-type semiconductor and an n-type semiconductor region. It can be used as a RF switch as its switching time is of order of microseconds.

give a single combined output. This single output represents the combined output of 8 dipoles. The output from three such parts (combined output of 8 dipoles) is further fed to a 3-way combiner. The output of 3 way combiner represent the combined output of 24 dipoles(half-module). Figure 2.4.2 shows a schematic of the combining network for half module[31].
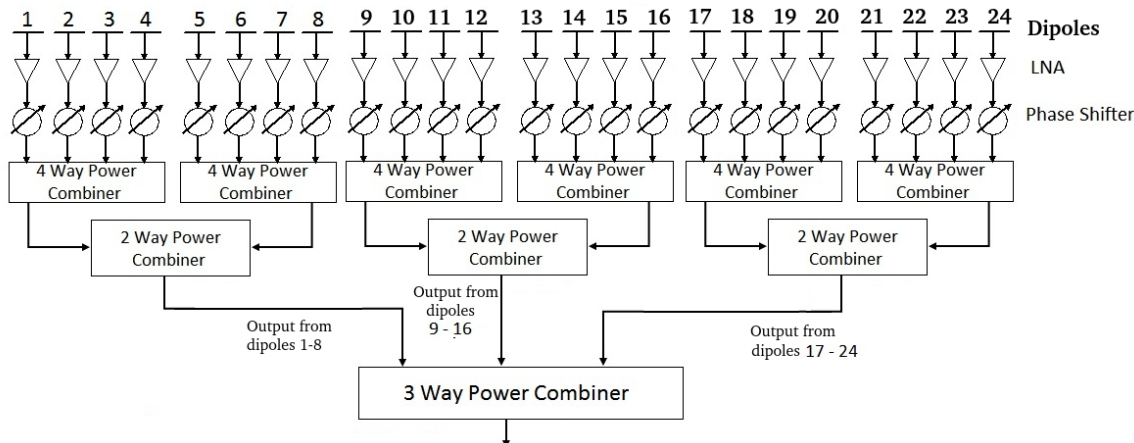
Figure 2.4.2: A schematic of a half-module of ORT showing a combined output of 24 dipoles[31].

The output from the two halves of the module are combined using a 2-way power combiner. The combined output of 48 dipoles is first amplified by a RF amplifier and then fed to a mixer (see fig.2.4.1) which downconverts the signal to a 30 MHz IF signal.

Mixer

Mixer employs a Local oscillator of frequency 296.5 MHz. It produces an IF signal of frequency $\nu_{sig} - \nu_{LO}$ where ν_{sig} is the frequency of input signal (326.5 MHz) and ν_{LO} is the frequency of Local Oscillator. This IF signal is amplified and then carried to the receiver room via co-axial transmission lines (see fig.2.4.1). In order to maintain phase symmetry in the array, all the dipoles are connected with equal lengths of the cables.

All devices in a module viz. LNA, Phase Shifter, 4-way, 3-way & 2-way combiners are of 50Ω impedance. The overall system noise temperature of the array is 150 K, assuming sky temperature is 40 K at 327 MHz[31].

2.4.2 ORT Back End

All the electronic systems in the receiver room are referred to as ORT Back End. Signals from each module are carried to the receiver room via co-axial transmission lines, where these signal can be correlated or added in phase to obtain phase switched beams or total power beams respectively. Fig.2.4.3 shows the block diagram of ORT receiver system.
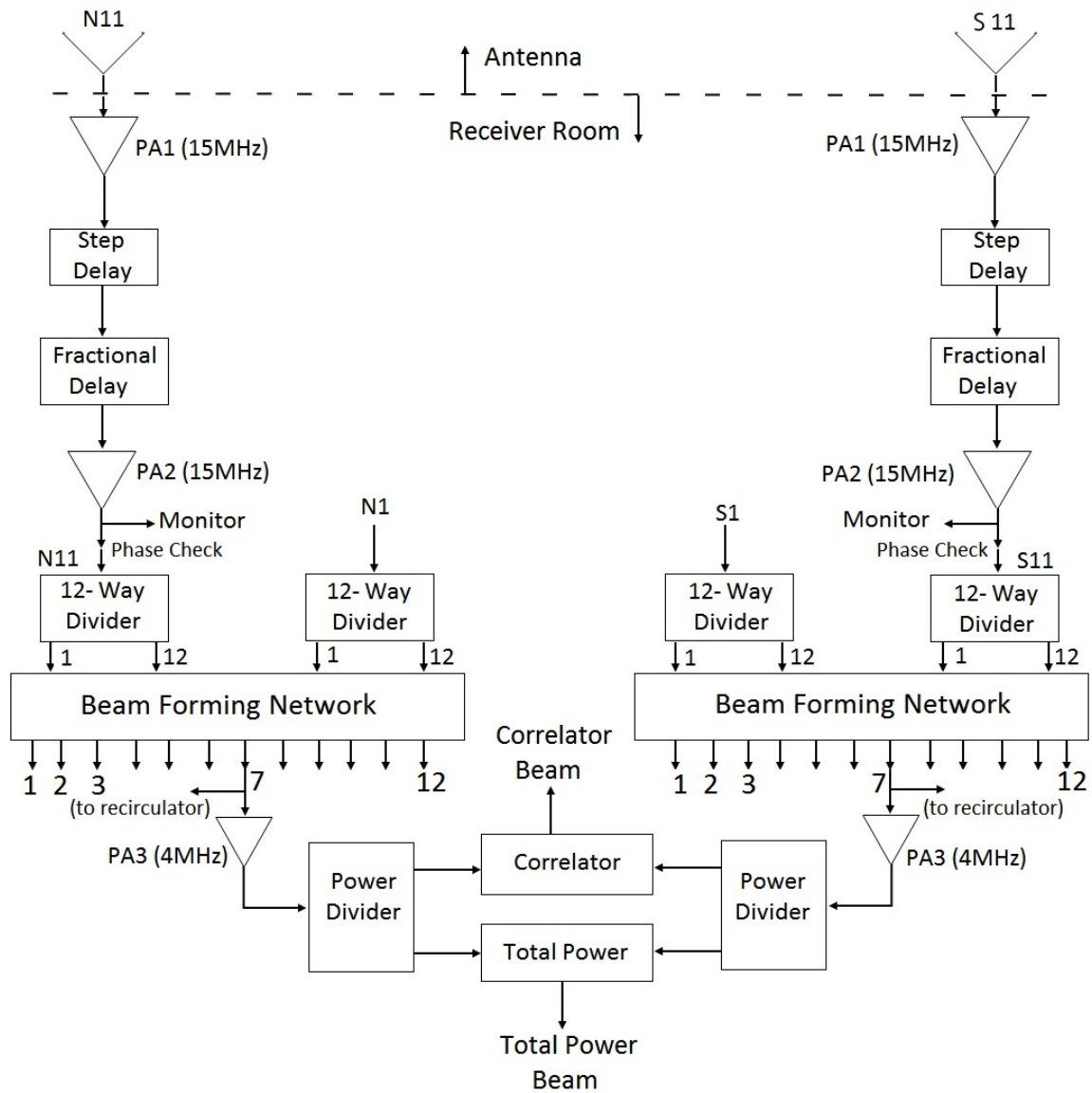
Figure 2.4.3: Block diagram of ORT receiver system.

IF Amplifiers

Signals from each module are amplified first by a post-IF amplifier PA1, to compensate for the signal loss in the cables between the antenna and the receiver room and then again in Post-IF amplifier PA2 which comes after the delay lines. PA2 compensates for the loss by the delay lines (see fig. 2.4.3)[30].

Delay control system (6-bit LO Phase Shifter)

As mentioned earlier, the 48 dipoles in an individual module are phased using the 4-bit phase shifters. In order to phase all the 1056 dipoles in the desired direction, it is also necessary to introduce appropriate delay and phase for each module before combining them. These phase and delays are introduced in the 30MHz IF path for each module (see fig.2.4.3). There is a limitation that the delays can be introduced only in integral multiples of IF wavelength since fractional wavelength will introduce a phase shift. For operation with wider bandwidth (> 2 MHz), it is necessary to set exact delays. The exact delays can be set in IF provided the phase shifts indroduced are compensated. For this purpose, 22 numbers of 6-bit phase shifters at LO frequency of 296.5 MHz are incorporated for each module of ORT. The actual delays are introduced in the IF while maintaining the phase coherence over the bandwidth by introducing the appropriate phases for every module at the LO frequency. This feature allows observations over a wide frequency range 320-334 MHz[30].

Phase Shifter Control and Monitor

The 48 dipoles on each of the 22 modules of the telescope are controlled by a digital Control & Monitor (C & M) system. The C & M system consists of a synchronous data link control based on programmable protocol controller on each module and a central PC. It sets the required bit pattern corresponding to the declination pointing.

The C & M system also has a provision to set the transmit/terminate bit for each dipole independently. Therefore any dipole can be connected to or disconnected from the array. In order to reduce the hardware with control and monitor system, the phase shifters for the two halves of each module consisting of 24 dipoles have been built such that the north and south halves are complementary. Thus, for phase shifter part, the control pattern consists of 92 bits[31].

Multiple Beam Forming

Twelve beams are formed for the north and south halves of the antenna separately using appropriate delays. Each PA2 output signal from the 11 north and 11 south modules is divided into 12 equal parts labelled $m = 1$ to 12 , using a resistive divider and transformer matching network. All m^{th} outputs from each resistive divider in one half of the module after being applied with appropriate delays are combined to form m^{th} beam[31]. Figure 2.4.4 represents the north half of the beam forming network.
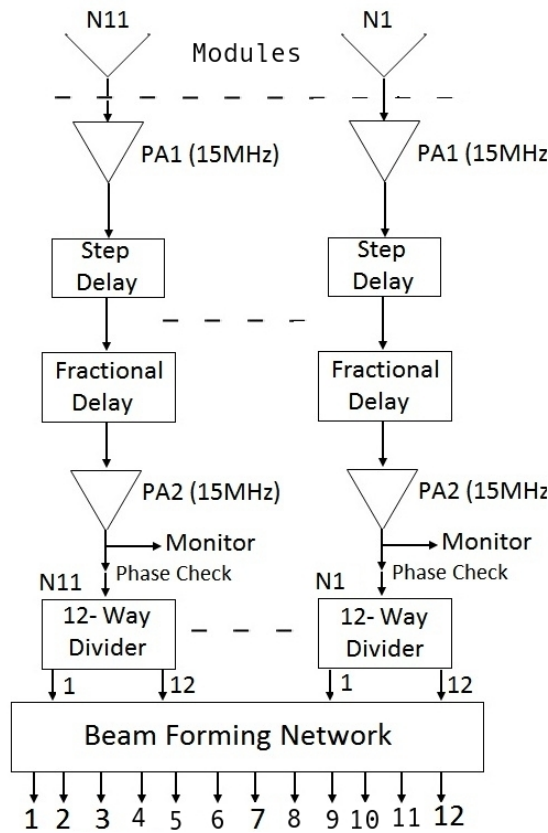
Figure 2.4.4: Block diagram of the north half of beam forming network[30].

Phase switched and total power beams

The outputs from the 12 beams for the 11 north and 11 south modules are connected to 12 correlators which give rise to the phase switched beams. The same signal is also added in phase to give 12 total power outputs corresponding to 12 beams (see fig. 2.4.3).

2.4.3 Performance of the Legacy system

The gain and phase stability of ORT feed is very good and gives a signal to noise ratio of 25.5 per Jy in the phase switched (between the north and the south halves of ORT) mode for a bandwidth of 4 MHz for 1 second integration time. The feed has the provision for selecting any one of the dipoles in a module, therefore it is possible to multiply just one dipole in one half of the telescope with the other half(528 dipoles) of the telescope and we get snr $\sim 1Jy$ for 10 msec integration. By tracking a strong celestial source (flux density > 50 Jy) and by switching in one dipole at a time the performance of each dipole can be recorded. Such tests have shown that feed has nearly uniform illumination (within ± 0.25 dB) over entire array[31].

2.4.4 Observations with the existing system

Low frequency radio astronomy provides excellent probes for many astrophysical phenomena. The large collecting area of ORT and its sensitivity makes it a powerful telescope for observations in metre wavelengths. Some of the observations are discussed in this section.

Pulsars

Pulsars are highly magnetized, rotating neutron stars(highly dense celestial bodies with mass $M \sim 1M_\odot$ and radius $r \sim 10$ Km) that emit beams of electromagnetic radiation from their magnetic poles. The time period of rotation of different pulsars can vary from milliseconds to seconds. Pulsars may be useful to resolve some of the fundamental problems in astrophysics, including gravitational background radiation, test for General theory of relativity, stellar evolution etc.

Individual pulses of millisecond pulsars can be seen with the help of ORT. For detection of weak pulsars higher integration times are required. The abrupt turn off of pulsar signal is known as nulling. With ORT, nulling of pulsars can be studied with high dynamic range, i.e. pulse intensity as low as $< 1\%$ of peak can be detected during nulling. Other observations include monitoring the scintillation characteristics and timing of individual pulsars.

Spectral line Observations

Spectral lines are extremely useful to study physical conditions and kinematics of gas in galaxies and clusters of galaxies. Redshifted 21 cm line (1420 MHz) of neutral hydrogen can be observed at ORT in band 320-334 MHz from the galaxies at redshift of ~3.35. Detection of 21 cm emission at these redshifts can tell about the history of galaxy formation[34][37].

Spectral lines corresponding to the atomic transitions between energy levels corresponding to $n_1 \sim 274, 273$ ... and $n_1 \sim 273, 272...$ respectively lie within the frequency band observable with ORT. These emission lines can originate from extremely low density gas at temperature~5000K. Observing these emission lines is an excellent probe to study such low density regions[1].

Interplanetary Scintillations (IPS) and Solar Winds

When radio waves of metre wavelengths propagate through interplanetary medi-um, it disrupts the wavefront of the wave which results in the fluctuation of the intensity of waves from distant compact radio sources. It is possible to derive both solar wind densities and velocities from the scintillation power spectra obtained using ORT.

Due to high sensitivity of ORT, it is possible to observe a large number of sources around the sun and map velocities and density of solar wind using the scintillation characteristics obtained by observing thess sources. Using this technique, any interplanetary disturbances detected by IPS can be traced back onto sun[23].

2.5   Interferometry and Aperture Synthesis

2.5.1   Signals in Radio Astronomy

A fundamental property of the radio waves emitted by cosmic sources is that they are stochastic in nature due to incoherence (random fluctuations in amplitude and phase), i.e. the electric field at Earth due to a distant cosmic source can be treated as a random process. Random processes can be simply understood as a generalization of random variables.

A commonly used statistic for random processes is the auto-correlation function. The auto-correlation function is defined as

$$r_{xx}(t, \tau) = \langle x(t)x(t + \tau) \rangle$$

where the angular brackets indicate taking the mean value. For a particularly important class of random processes, the auto-correlation function is independent of changes of the origin of t and is a function of τ alone, these processes are known as called wide sense stationary (WSS) processes i.e.

$$r_{xx}(\tau) = \langle x(t)x(t + \tau) \rangle \tag{2.17}$$

For $\tau = 0, r(\tau)$ is simply the variance σ^2 of $x(t)$. The Fourier transform of the auto-correlation function $r_{xx}(\tau)$ is called the power spectrum $(S(\nu))$, i.e.

$$S(\nu) = \int_{-\infty}^{\infty} r_{xx}(\tau)e^{-i2\pi\nu\tau}d\tau \tag{2.18}$$

Equivalently, $S(\nu)$ is the inverse Fourier transform of $r(\tau)$ or

$$r_{xx}(\tau) = \int_{-\infty}^{\infty} S(\nu)e^{i2\pi\nu\tau}d\nu \tag{2.19}$$

Hence,

$$r_{xx}(0) = \sigma^2 = \int_{-\infty}^{\infty} S(\nu)d\nu \tag{2.20}$$

since σ^2 is the "power" in the signal, $S(\nu)$ describes how that power is distributed in frequency space, i.e. the "power spectrum".

A process whose auto-correlation function is a delta function has a power spectrum that is flat – such a process is called "white noise". Many radio astronomical signals have spectra that are relatively flat, therfore these signals can be approximated as white noise. Radio astronomical receivers however have limited bandwidths, that means that even if the signal input to the receiver is white noise, the signal after passing through the receiver has power only in a finite frequency range. Its auto-correlation function is hence no longer a delta function, but is a sinc function with a width $\sim 1/\Delta\nu$, where $\Delta\nu$ is the bandwidth of the receiver. The width of the auto-correlation function is also called the "coherence time" of the signal. The signals for for which bandwidth $\Delta\nu$ is typically much smaller than the central frequency ν are

known as quasi-monochromatic signals and can be represented using complex random processes.

Given two random processes $x(t)$ and $y(t)$, one can define a cross-correlation function

$$r_{xy}(\tau) = \langle x(t)y(t-\tau)\rangle$$

Here we assumed that the signals are WSS so that the cross-correlation function is a function of τ alone.

The signal received from a distant cosmic source is in general a function both of the receivers location as well as of time. Similar to temporal correlation functions, spatial correlation functions can also be defined. If the signal at the observer's plane at any instant is E($\mathbf{r}$), then spatial correlation function is defined as:

$$V(\mathrm{x}) = \langle E(\mathrm{r})E^*(\mathrm{r} + \mathrm{x})\rangle \tag{2.21}$$

Note that the angular brackets imply ensemble averaging. In practice one averages over time and assumes that the two averaging procedures are equivalent. The function V is referred to as the "visibility function" (or just the "visibility") and is of fundamental interest in interferometry.

2.5.2   The need for Interferometry

The resolution of optical instruments is limited due to Rayleigh's criterion which states that the angular resolution of a telescope/microscope is ultimately diffraction limited and this limit is given by

$$\theta \sim \lambda/D \ , \tag{2.22}$$

where D is some measure of the aperture size. To achieve higher resolutions(smaller θ) one has to either increase the diameter of the telescope further or decrease the observing wavelength. To achieve high angular resolutions at metre wavelengths one needs telescopes with apertures that are hundreds of kilometers in size. Single telescopes of this size are clearly impossible to build. To achieve such resolutions a technique called aperture synthesis is used which is based on interferometry. There is a deep analogy between the double slit experiment with quasi-monochromatic light and the two element radio interferometer.

2.5.3 Van Cittert Zernike Theorem

The van Cittert-Zernike theorem relates the spatial coherence function (Eq. 2.21) to the distribution of intensity of the incoming radiation, $\mathcal{I}(\mathbf{s})$. It shows that the spatial correlation function $V(\mathbf{r_1}, \mathbf{r_2})$ depends only on $\mathbf{r_1} - \mathbf{r_2}$ and if all the measurements are in a plane, then

$$V(\mathbf{r_1}, \mathbf{r_2}) = \mathcal{F}\{\mathcal{I}(\mathbf{s})\} \tag{2.23}$$

where $\mathcal{F}$ implies taking the Fourier transform.
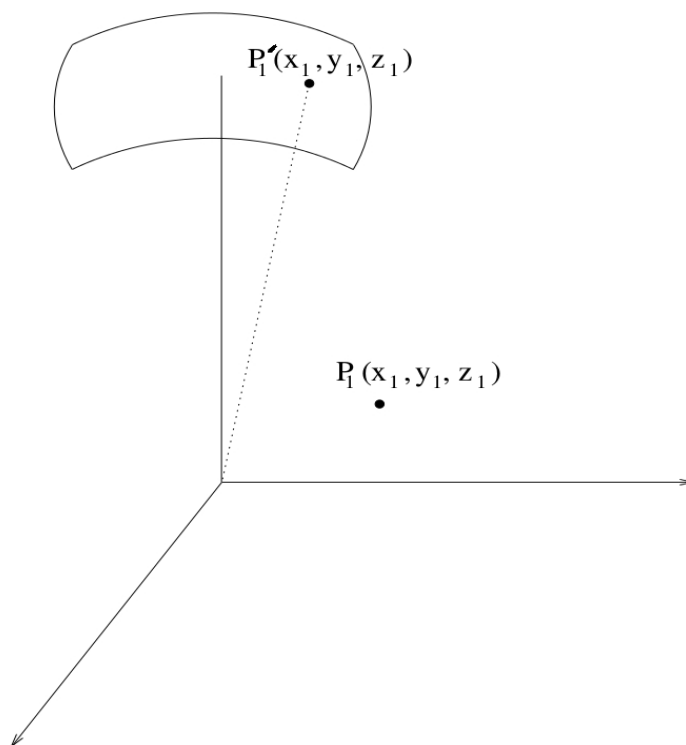
Figure 2.5.1: Geometry for Van Cittert Zernike theorem.

Let us assume that the source is distant and can be approximated as a brightness distribution on the celestial sphere of radius R (see Figure 2.5.1). Let the electric field at a point $P_1'(x_1', y_1', z_1')$ at the source be given by $\mathcal{E}(P_1')$. The field $E(P_1)$ at the observation point $P_1(x_1, y_1, z_1)$ is given by

$$E(P_1) = \int \mathcal{E}(P_1') \frac{e^{-ikD(P_1', P_1)}}{D(P_1', P_1)} d\Omega_1 \tag{2.24}$$

where $D(P_1', P_1)$ is the distance between P_1' and P_1.

Similarly if $E(P_2)$ is the field at some other observing point $P_2(x_2, y_2, z_2)$ then the cross-correlation between these two fields is given by

$$\langle E(\mathrm{P}_1)E^*(\mathrm{P}_2)\rangle = \int \langle \mathcal{E}(P_1')\mathcal{E}^*(P_2')\rangle \frac{e^{-ik\left[D(P_1',P_1)-D(P_2',P_2)\right]}}{D(P_1',P_1)D(P_2',P_2)}d\Omega_1 d\Omega_2 \tag{2.25}$$

If we further assume that the emission from the source is spatially incoherent, i.e. that $\langle \mathcal{E}(P_1')\mathcal{E}^*(P_2')\rangle = 0$ except when $P_1' = P_2'$, then we have

$$\langle E(\mathrm{P}_1)E^*(\mathrm{P}_2)\rangle = \int \mathcal{I}(P_1') \frac{e^{-ik\left[D(P_1',P_1)-D(P_1',P_2)\right]}}{D(P_1',P_1)D(P_1',P_2)}d\Omega_1 \tag{2.26}$$

where $\mathcal{I}(P_1')$ is the intensity at the point P_1'. Since we have assumed that the source can be approximated as lying on a celestial sphere of radius R we have $x_1 = R\cos(\theta_x) = Rl, y_1 = R\cos(\theta_y) = Rm$, and $z_1 = R\cos(\theta_z) = Rn$; (l, m, n) are called "direction cosines". It can be easily shown that $l^2 + m^2 + n^2 = 1$ and $d\Omega = \dfrac{dldm}{\sqrt{1 - l^2 - m^2}}$. We then have:

$$D(P_1', P_1) = [(x_1' - x_1)^2 + (y_1' - y_1)^2 + (z_1' - z_1)^2]^{1/2} \tag{2.27}$$

$$= [(Rl - x_1)^2 + (Rm - y_1)^2 + (Rn - z_1)^2]^{1/2} \tag{2.28}$$

$$= R[(l - x_1/R)^2 + (m - y_1/R)^2 + (n - z_1/R)^2]^{1/2} \tag{2.29}$$

$$\simeq R[(l^2 + m^2 + n^2) - \frac{2}{R}(lx_1 + my_1 + nz_1)]^{1/2} \tag{2.30}$$

$$\simeq R[1 - \frac{1}{R}(lx_1 + my_1 + nz_1)] \quad \text{(using binomial expansion)} \tag{2.31}$$

$$= R - (lx_1 + my_1 + nz_1) \tag{2.32}$$

Putting this into Equation 2.26 we get,

$$\langle E(\mathrm{P}_1)E^*(\mathrm{P}_2)\rangle = \frac{1}{R^2} \int \mathcal{I}(l, m) e^{-ik[l(x_2 - x_1) + m(y_2 - y_1) + n(z_2 - z_1)]} \frac{dldm}{\sqrt{1 - l^2 - m^2}} \tag{2.33}$$

Note that since $l^2 + m^2 + n^2 = 1$, the two directions cosines (l, m) are sufficient to uniquely specify any given point on the celestial sphere, which is why the intensity $\mathcal{I}$ has been written out as a function of (l, m) only. Distances in the observing plane are measured in units of the wavelength λ, and define "baseline co-ordinates" u, v, w such that $u = (x_2 - x_1)/\lambda$, $v = (y_2 - y_1)/\lambda$, and $w = (z_2 - z_1)/\lambda$. The spatial correlation function $\langle E(\mathrm{P}_1)E^*(\mathrm{P}_2)\rangle$ is also referred to as the "visibility" $V(u, v, w)$. Equation

2.33 (ignoring $1/R^2$ term) can be written as

$$\mathcal{V}(u,v,w) = \int \frac{\mathcal{I}(l,m)}{\sqrt{1-l^2-m^2}} e^{-i2\pi[lu+mv+nw]} dl\, dm \qquad (2.34)$$

This fundamental relationship between the visibility and the source intensity distribution is the basis of radio interferometry. Equation 2.34 is also referred to as Van Cittert Zernike theorem. Equation 2.34 resembles a Fourier transform. There are two situations in which it does reduce to a Fourier transform. The first is when the observations are confined to the $u-v$ plane, i.e. when $w=0$. In this case we have

$$\mathcal{V}(u,v) = \int \frac{\mathcal{I}(l,m)}{\sqrt{1-l^2-m^2}} e^{-i2\pi[lu+mv]} dl\, dm \qquad (2.35)$$

i.e. the visibility $\mathcal{V}(u,v)$ is the Fourier transform of the modified brightness distribution $\frac{\mathcal{I}(l,m)}{\sqrt{1-l^2-m^2}}$.

The second situation is when the source brightness distribution is limited to a small region of the sky. In this case $n^2 = 1 - l^2 - m^2 \simeq 1$. Equation 2.34 then becomes

$$\mathcal{V}(u,v,w) = e^{-i2\pi w} \int \mathcal{I}(l,m) e^{-i2\pi[lu+mv]} dl\, dm \qquad (2.36)$$

If we define a modified visibility $\widetilde{\mathcal{V}}(u,v) = \mathcal{V}(u,v,w) e^{i2\pi w}$, we have

$$\widetilde{\mathcal{V}}(u,v) = \int \mathcal{I}(l,m) e^{-i2\pi[lu+mv]} dl\, dm \qquad (2.37)$$

2.5.4   Aperture Synthesis

In previous section we saw that the spatial correlation of the electric field in the $u-v$ plane is related to the source brightness distribution. For a typical radio array the relationship between the measured visibility and the source brightness distribution is a simple Fourier transform. Thus, Correlation of the voltages from any two radio antennas allows the measurement of a single Fourier component of the source brightness distribution. Given sufficient number of measurements, the source brightness distribution can then be obtained by Fourier inversion. The derived image of the sky is usually called a "map", and the process of producing the image from the visibilities is called "mapping".

The radio sky (apart from a few rare sources) does not vary. This means that it is not necessary to measure all the Fourier components simultaneously. Only two
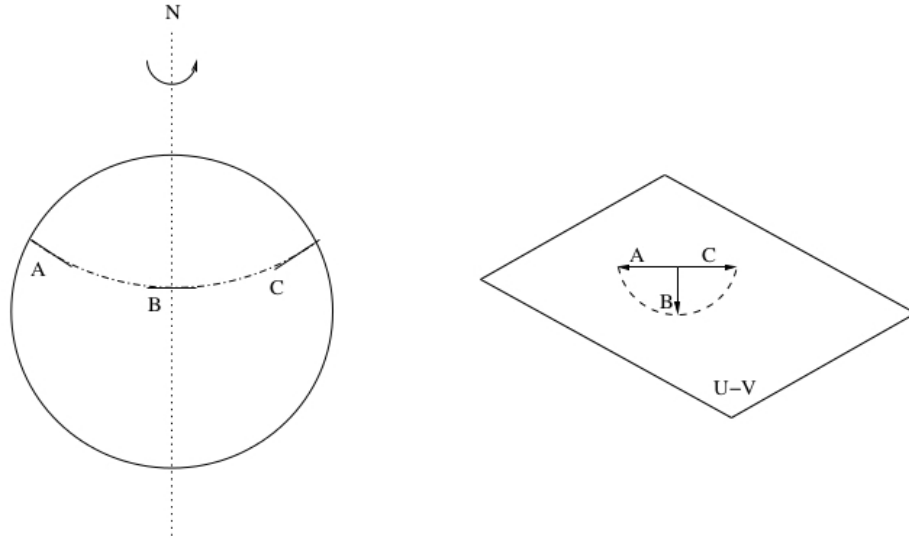
Figure 2.5.2: The track in the $u - v$ plane traced out by an east-west baseline due to the Earth's rotation[14].

antennas can be used to measure all required fourier components, this can be done by changing the separation between the antennas and measuring the fourier componenent for each separation. This method of building up all the required Fourier components and using them to image the source is called "aperture synthesis". For example, if one has measured all Fourier components up to a baseline length of say 500 m, then one could obtain an image of the sky with the same resolution as that of a telescope of aperture size 500 m, i.e. one has synthesized a 500 m aperture.

In practice, one can use the rotation of Earth to sample the $u - v$ plane quite rapidly. As seen from a distant cosmic source, the baseline vector between two antennas on the Earth changes continuously because of Earth's rotation (see Figure 2.5.2). As the source rises and sets, the Fourier components measured by a given pair of antennas changes continuously. If an array of N antennas is spread on the Earth's surface, then at any given instant $^{N}C_2$ Fourier components can be measured. As the Earth rotates one samples more and more of the $u - v$ plane. This technique of using the Earth's rotation to improve $u - v$ coverage is referred to as "Earth rotation aperture synthesis". Full synthesis $u - v$ coverage of GMRT is shown in figure 2.5.3. However, earth rotation aperture synthesis can not be performed for an equatorial mount interferometer because its baselines do not change with earth's rotation and $u - v$ plane consists of fixed number of points rather than smooth curves.

From the inverse relationship of Fourier conjugate variables it follows that short baselines are sensitive to large angular structures in the source and that long baselines
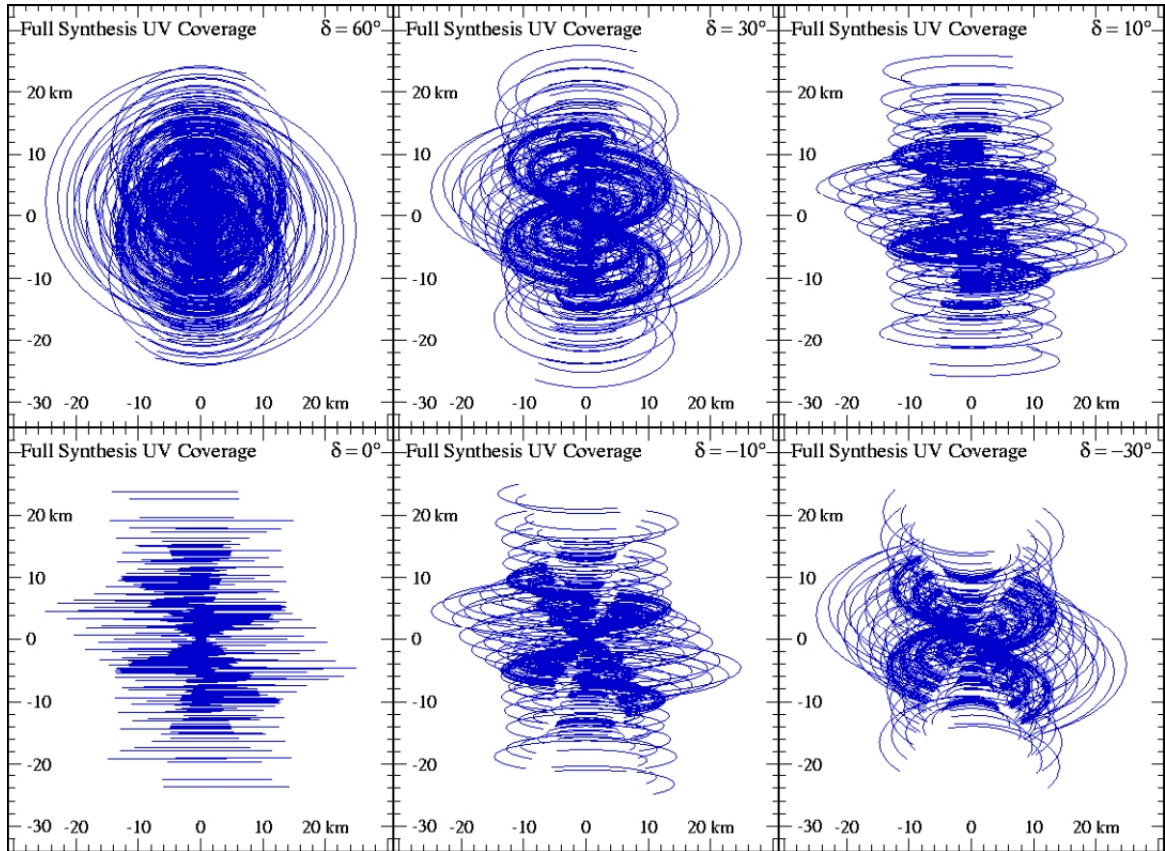
Figure 2.5.3: Full synthesis $u - v$ coverage of full GMRT array at various declinations indicated in each panel[45].

aresensitive to fine scale structure. An array with the antennas which are closely packed together can be used to image large, smooth sources, while for a source with considerable fine scale structure one needs antennas spread out to large distances. Therefore, the array configuration has a major influence on the kind of sources that can be imaged.

2.5.5   Two-element Interferometer

From the van-Cittert Zernike theorem (Eq. 2.34, 2.35, 2.37) it follows that if one knows the mutual coherence function of the electric field, then the source brightness distribution can be measured. In this section we will discuss how the mutual coherence function is measured.

Consider a two element interferometer shown in Figure 2.5.4. Two antennas with baseline vector $\mathbf{b}$, are directed towards a point source of flux density S. The angle between the direction to the point source and the normal to basline vector is θ. The
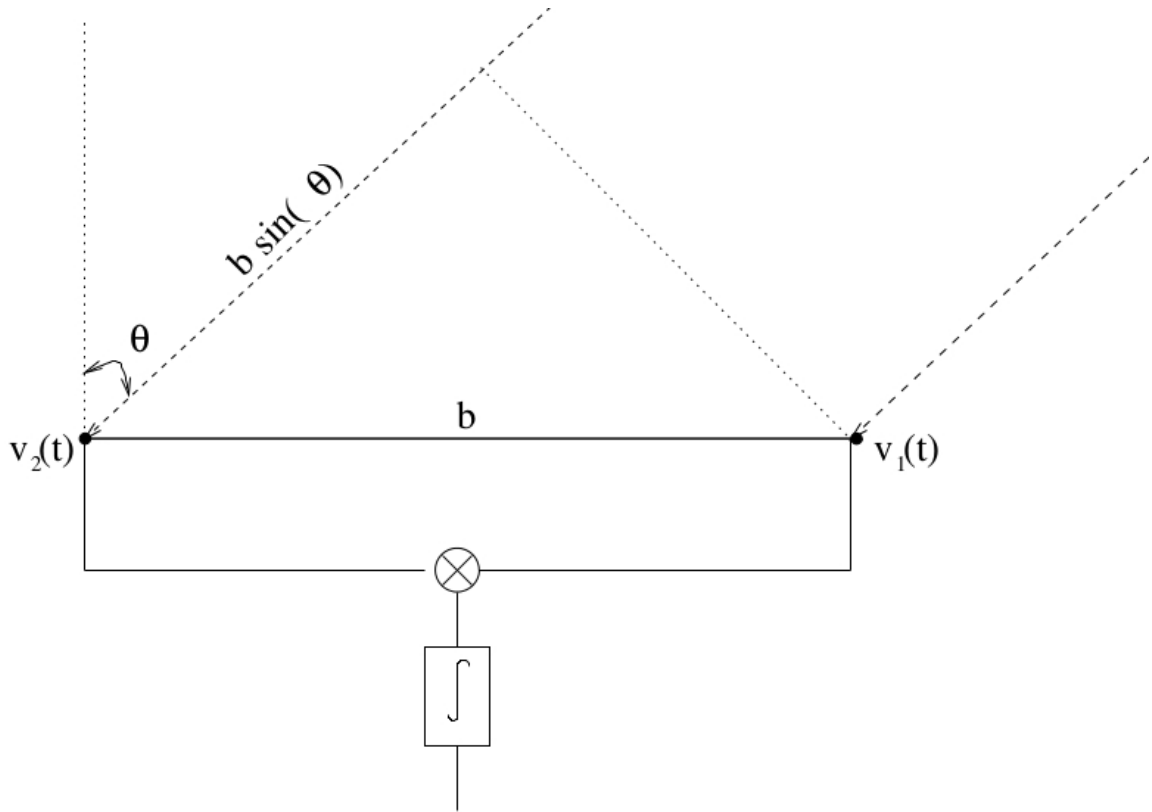
Figure 2.5.4: A basic two-element interferomter[14].

voltages that are produced at the two antennas due to the electric field from this point source are $v_1(t)$ and $v_2(t)$ respectively. These two voltages are multiplied together, and then averaged. Assume that the radiation emitted by the source is monochromatic and has frequency ν and voltage at antenna 1 be

$$v_1(t) = \cos(2\pi\nu t)$$

Since the radio waves from the source have to travel an extra distance $b\sin\theta$ to reach antenna 2, the voltage there is delayed by the amount $b\sin\theta/c$. This is called the geometric delay, τ_g. The voltage at antenna 2 is hence

$$v_2(t) = \cos(2\pi\nu(t - \tau_g))$$

where we have assumed that the antennas have identical gain. The averaged output of the multiplier is given by

$$r(\tau_g) = \frac{1}{\mathrm{T}} \int_{t-T/2}^{t+T/2} \cos(2\pi\nu t)\cos(2\pi\nu(t-\tau_g))dt \qquad (2.38)$$

$$= \frac{1}{\mathrm{T}} \int_{t-T/2}^{t+T/2} (\cos(4\pi\nu t - 2\pi\nu\tau_g) + \cos(2\pi\nu\tau_g))dt \qquad (2.39)$$

$$= \cos(2\pi\nu\tau_g) \qquad (2.40)$$

assuming that the averaging time T is long compared to $1/\nu$. The $\cos(4\pi\nu t)$ factor hence averages out to zero. As the source rises and sets, the angle θ changes. If we assume that baseline vector is exactly east west, and that the source's declination $\delta_0 = 0$, then $\theta = \Omega_E t$, (where Ω_E is the angular frequency of the earth's rotation) we have:

$$r(\tau_g) = \cos(2\pi\nu \times b/c \times \sin(\Omega_E(t-t_z))) \qquad (2.41)$$

where t_z is the time at which the source is at the zenith. The output $r(\tau_g)$, (also called the fringe), hence varies in a quasi-sinusoidal form, with its instantaneous frequency being maximum when the source is at zenith and minimum when the source is either rising or setting (Figure 2.5.5).
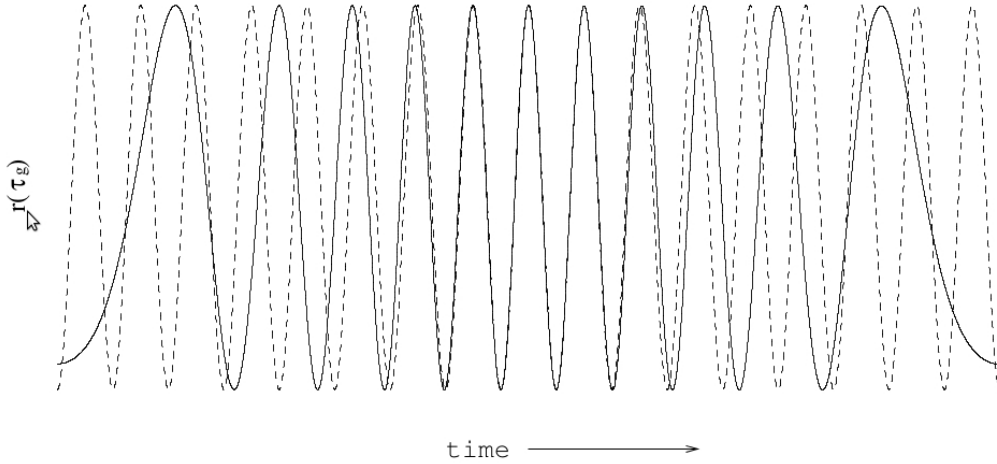
Figure 2.5.5: The output of a two element interferometer as a function of time. The solid line is the observed qausi-sinosoidal output (the fringe), the dotted line is a pure sinusoid whose frequency is equal to the peak instantaneous frequency of the fringe. The instantaneous fringe frequency is maximum when the source is at the zenith (the center of the plot) and is minimum when the source is rising (left extreme) or setting (right extreme)[14].

If the source's right ascension was known, then one could compute the time at which the source would be at zenith, and hence the time at which the instantaneous fringe frequency would be maximum. If the fringe frequency peaks at some slightly different time, then assumed right ascension of the source is slightly in error from the actual one. Thus, in principle, from the difference between the actual observed peak time and the expected peak time, the true right ascension of the source can be determined.

Similarly, if the source were slightly extended (assuming uniform brightness distribution), then when the waves from a given point on the source arrive in phase at the two ends of the interferometer, waves arising from adjacent points on the source will arrive slightly out of phase. The observed fringe amplitude will be less than that for a point source of the same total flux. The more extended the source, the lower the fringe amplitude. For sufficiently large source with smooth brigtness distribution, the fringe amplitude will be essentially zero. In such circumstances, the interferometer is said to have resolved out the source.

Further, two element interferometers cannot distinguish between sources whose sizes are small compared to the fringe spacing, all such sources will appear as point sources. Thus, the minimum source size that can be resolved by the interferometer is

$$\pi \nu \Delta\theta b/c \lesssim \pi \implies \Delta\theta \lesssim \lambda/b \tag{2.42}$$

i.e., the resolution of a two element interferometer is $\sim \lambda/b$. The longer the baseline, the higher the resolution. Observations with a two element interferometer hence give information on both the source position and the source size.

2.5.6 Interferometer response to Quasi-monochromatic radiation

Till now we had assumed that the radiation from the source was monochromatic. Let us now consider the case of quasi-monochromatic radiation, i.e. the radiation spectrum contains all frequencies in a band $\Delta\nu$ around ν, with $\Delta\nu$ small compared to ν. If the radiation at some frequency ν arrives in phase at the two antennas in the interferometer, the radiation at some adjacent frequencies will arrive out of phase. Hence, averaging over all these frequencies would decrease the amplitude of the fringe. We have (Eq. 2.40):

$$r(\tau_g) = \frac{1}{\Delta \nu} \int_{\nu - \Delta \frac{\nu}{2}}^{\nu + \Delta \frac{\nu}{2}} \cos(2\pi\nu\tau_g) d\nu \qquad (2.43)$$

$$= \frac{1}{\Delta \nu} Re \left[\int_{\nu - \Delta \nu/2}^{\nu + \Delta \nu/2} e^{i2\pi\nu\tau_g} d\nu \right] \qquad (2.44)$$

$$= \cos(2\pi\nu\tau_g) \left[\frac{\sin(\pi\Delta\nu\tau_g)}{\pi\Delta\nu\tau_g} \right] \qquad (2.45)$$

The sinc function decreases rapidly with increasing bandwidth. Hence as the bandwidth that is accepted by the telescope is increased, the fringe amplitude decreases sharply. This is called fringe washing. Let us look at the fringe due to a spatially extended source. Let the direction vector to some reference point on the source be $\mathbf{s_0}$, and further assume that the source is small that it lies entirely on the tangent plane to the sky at $\mathbf{s_0}$, i.e. that the direction to any point on the source can be written as $\mathbf{s} = \mathbf{s_0} + \sigma$, $\mathbf{s_0}.\sigma = 0$, $\tau_g = \mathbf{s_0}.\mathbf{b}$. Then, from the van Cittert-Zernike theorem we have:

$$r(\tau_g) = Re \left[\int I(\mathbf{s}) e^{\frac{-i2\pi\mathbf{s}.\mathbf{b}}{\lambda}} d\mathbf{s} \right] \qquad (2.46)$$

$$= Re \left[e^{\frac{-i2\pi\mathbf{s_0}.\mathbf{b}}{\lambda}} \int I(\mathbf{s}) e^{\frac{-i2\pi\sigma.\mathbf{b}}{\lambda}} d\mathbf{s} \right] \qquad (2.47)$$

$$= |\mathcal{V}|\cos(2\pi\nu\tau_g + \Phi_\mathcal{V}) \qquad (2.48)$$

where $\mathcal{V}$ is the complex visibility and is defined as:

$$\mathcal{V} = |\mathcal{V}|e^{i\Phi_\mathcal{V}} = \int I(\mathbf{s}) e^{\frac{-i2\pi\sigma.\mathbf{b}}{\lambda}} d\mathbf{s} \qquad (2.49)$$

The information on the source size and structure is contained entirely in $\mathcal{V}$, the factor $\cos(2\pi\nu\tau_g)$ in Eq. (2.48) only contains the information that the source rises and sets as the earth rotates. Since this is trivial and uninteresting, it can safely be suppressed. This information can be suppressed by introducing an instrumental delay $\tau_i = \tau_g$ along the electrical signal path of antenna 1. This will provide $r(\tau_g) = |\mathcal{V}|\cos(\Phi_\mathcal{V})$, i.e. the fast fringe oscillation has been suppressed. Since τ_g changes with time as the source rises and sets, τ_i will also have to be continuously adjusted. The adjustment of τ_i is called delay tracking.
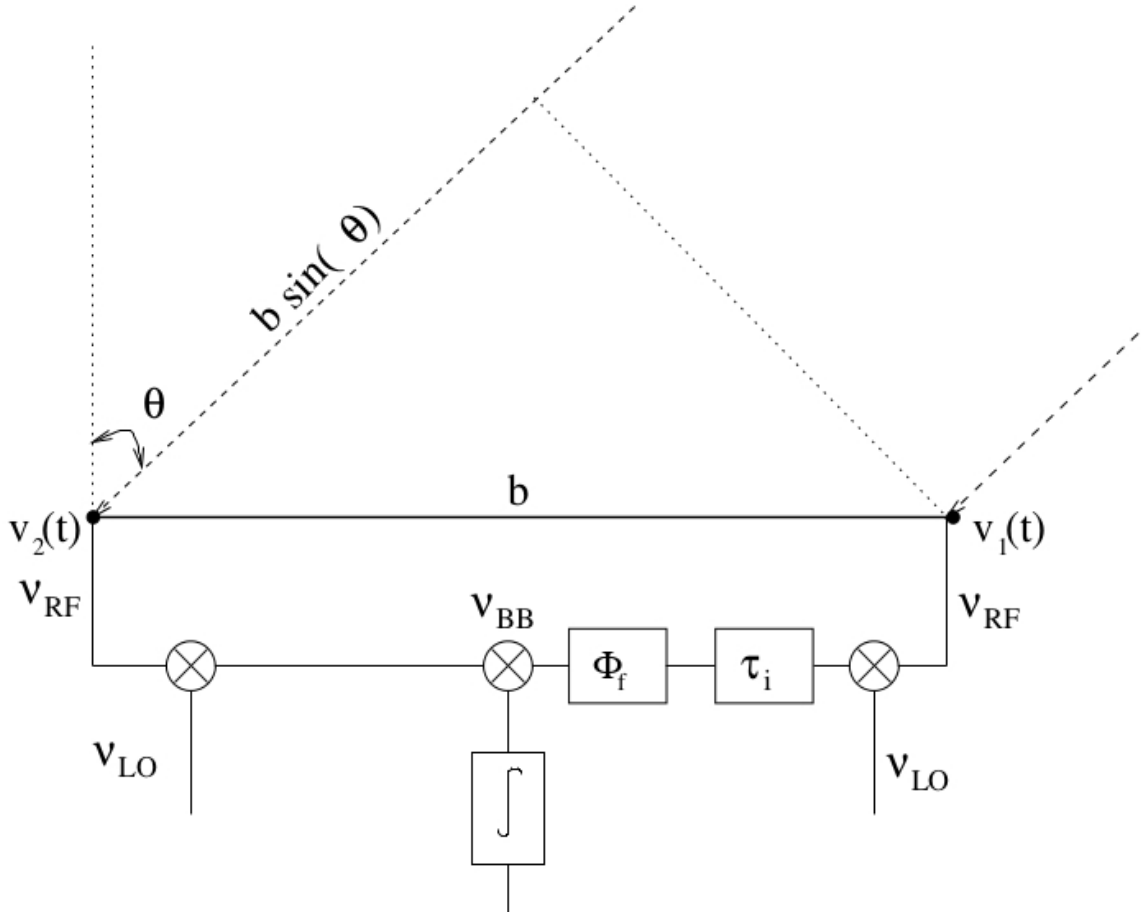
Figure 2.5.6: A 2-element interferometer with fringe stopping and delay tracking[14].

Let us consider the interferometer shown in Figure 2.5.6. The signals from antennas 1, 2 are first converted to a frequency ν_{BB} using a mixer which is fed using a local oscillator of frequency ν_{LO} , i.e.$\nu_{LO} = \nu_{RF} - \nu_{BB}$. Along the signal path for antenna 1 an additional instrumental delay $\tau_i = \tau_g + \Delta\tau$ and a time varying phase shift Φ_f is introduced. We have:

$$r(\tau_g) = |\mathcal{V}|\langle\cos(\Phi_\mathcal{V} + 2\pi\nu_{BB}t - 2\pi\nu_{RF}\tau_g)\cos(2\pi\nu_{BB}(t - \tau_i) + \Phi_f)\rangle \qquad (2.50)$$

$$= |\mathcal{V}|\cos(\Phi_\mathcal{V} + 2\pi(\nu_{RF} - \nu_{BB})\tau_g - 2\pi\nu_{BB}\Delta\tau - \Phi_f) \qquad (2.51)$$

$$= |\mathcal{V}|\cos(\Phi_\mathcal{V} + 2\pi\nu_{LO}\tau_g - 2\pi\nu_{BB}\Delta\tau - \Phi_f) \qquad (2.52)$$

So, in order to compensate for all time varying phase factors, it is not sufficient to have $\tau_i = \tau_g$, one also needs to introduce a time varying phase $\Phi_f = 2\pi\nu_{LO}\tau_g$. This additional correction arises because the delay tracking is done at a frequency different

from ν_{RF}. The introduction of the time varying phase is called fringe stopping.The delay tracking and fringe stopping corrections apply for a specific point in the sky, i.e. the position $\mathbf{s_0}$. This point is called the phase tracking center.

2.6 Upgraded System

The upgradation of ORT is in progress, after which the linear dipole array may be used as a radio interferometer. Upgradation is being carried out in two different stages with two nearly independent systems namely Phase **I** and Phase **II**, after which signal from an antenna element will be digitized directly and transmitted to the receiver room via fibre optic transmission rather than the analog transmisssion which was present in the old system, upgradation is being carried out such that the existing analog system remains as it is[8][27]. After the upgradation ORT will be able to provide larger instantaneous field of view, this will lead to new astronomical observations using ORT.

2.6.1 Phase I

In Phase I, 24 dipoles(half-module) are combined to form a single antenna element. The output signals are amplified, filtered, directly digitized in the field and the digitized data is transmitted via fibre optic cables to the receiver room. While there are 22 ORT modules(or 44-elements) but it may be noted that only 40 elements are interfaced to the upgraded digital receiver. The 2 modules at either end of the array (S11 and N11, north and south) are being used to carry out RF validation of various subsystems. Figure 2.6.3 reperesents the schematic view of the ORT 40 element interferometric array.

The upgraded module for Phase **I** caters to tapping the combined RF from the existing ORT RF frontend (see figure 2.6.1), conditioning the tapped RF for direct RF sampling, and feeding it into the new digital receiver. The RF signal conditioning is composed of two stages. In stage-1, the first stage of amplification (pre-amplifier) of the combined RF received from the RF frontend is carried out to compensate for cable losses during transmission of the RF from feed to base. In addition, a coupled port is provided to interface the RF frontend output to the existing analog system. The output of the coupled port is passed to the Data Acquisition System(DAS). Figure 2.6.2 represents a schematic of RF signal conditioning subsystem and Data Acquisition system at a pillar.
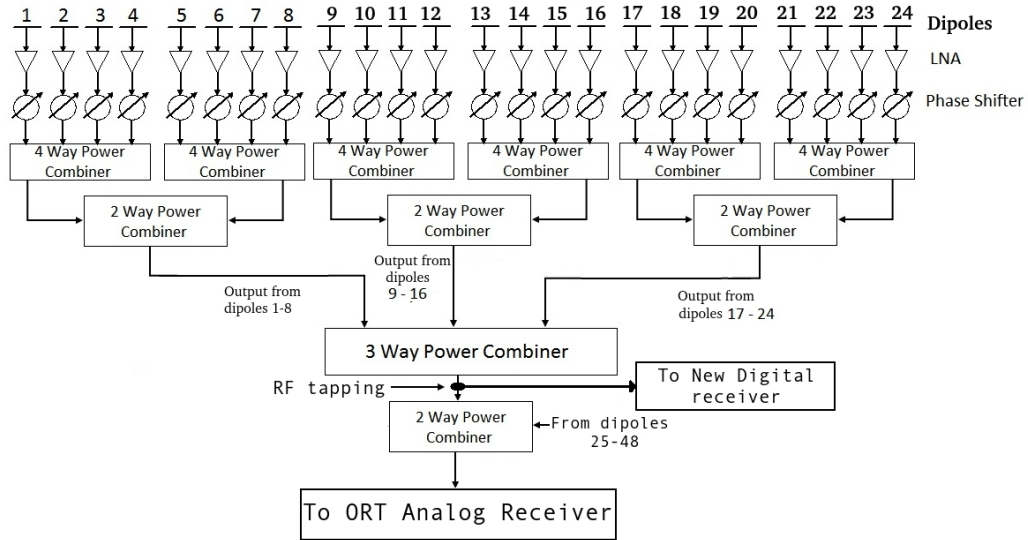
Figure 2.6.1: ORT sub-module for Phase **I**. The RF tapping location for the RF digital receiver is shown[27].
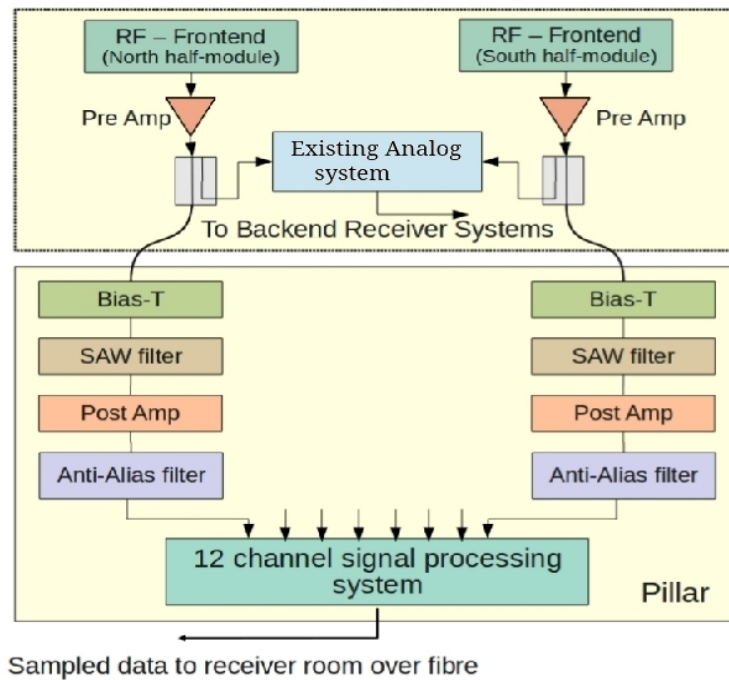
Figure 2.6.2: Data acquisition sub-system(at Pillar) for Phase **I**[27].

Data acquisition system for Phase I

The conditioned RF signal from an antenna element(half-module) is fed to a 12 channel Data Acquisition System(DAS) consisting of Analog to Digital Convertors(ADC) which caters to 10 analog inputs(Each input corresponds to an antenna element(half

module)) and sends out digitized data using optical fibre link(see figure 2.6.2). There are 4 Data Acquisition Systems in Phase **I** namely N08, N03, S08 & S03, which can handle data from 40 antenna elements (see figure 2.6.3). The remotely digitized data is ecapsulated in packets by the DAS boxes at the pillar and are sent to receiver room over a single, full duplex fibre optic link (2.5Gbps) based on Aurora protocol at full aurora bandwidth of 250MBps (see figure 2.6.2 & 2.6.3).
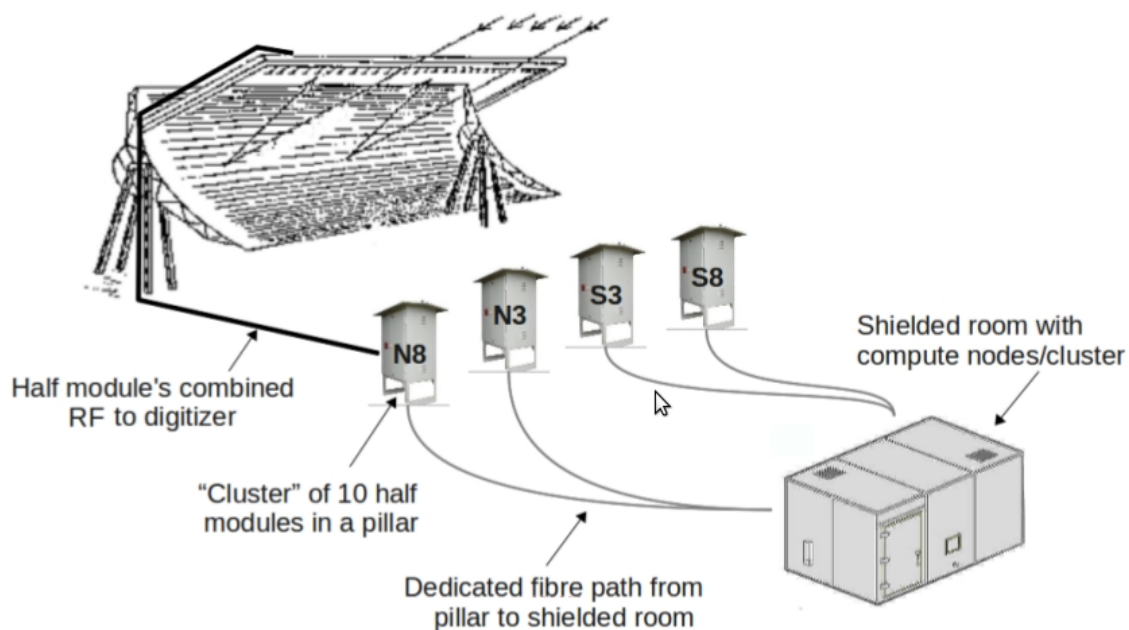
Figure 2.6.3: Schematic view of the ORT 40 element interferometric array, and its receiver. Each of the shown pillars handles 10 half module antenna elements, performing digitization, packetization, data transposition and timestamping of the data, before transmitting them over an optical fibre network to a central processor[27].

Receiver system for Phase I

The receiver system consists of a FPGA(Virtex-5) based pooler card, a pair of FPGA(Virtex-5) based bridge cards and two server class machines each having 4 Gigabit Ethernet links and a large memory.

The pooler card accepts the fibre optic inputs from the four DAS boxes (N08, N03, S03, S11) and generates four serial outputs on copper cables, connected pairwise to two bridge cards(see figure 2.6.4). Pooler acts as a pass through, routing the incoming data available over the Aurora links to a single bridge card. The bridge cards convert the incoming Aurora based data to Gigabit Ethernet(udp protocol) and produces two
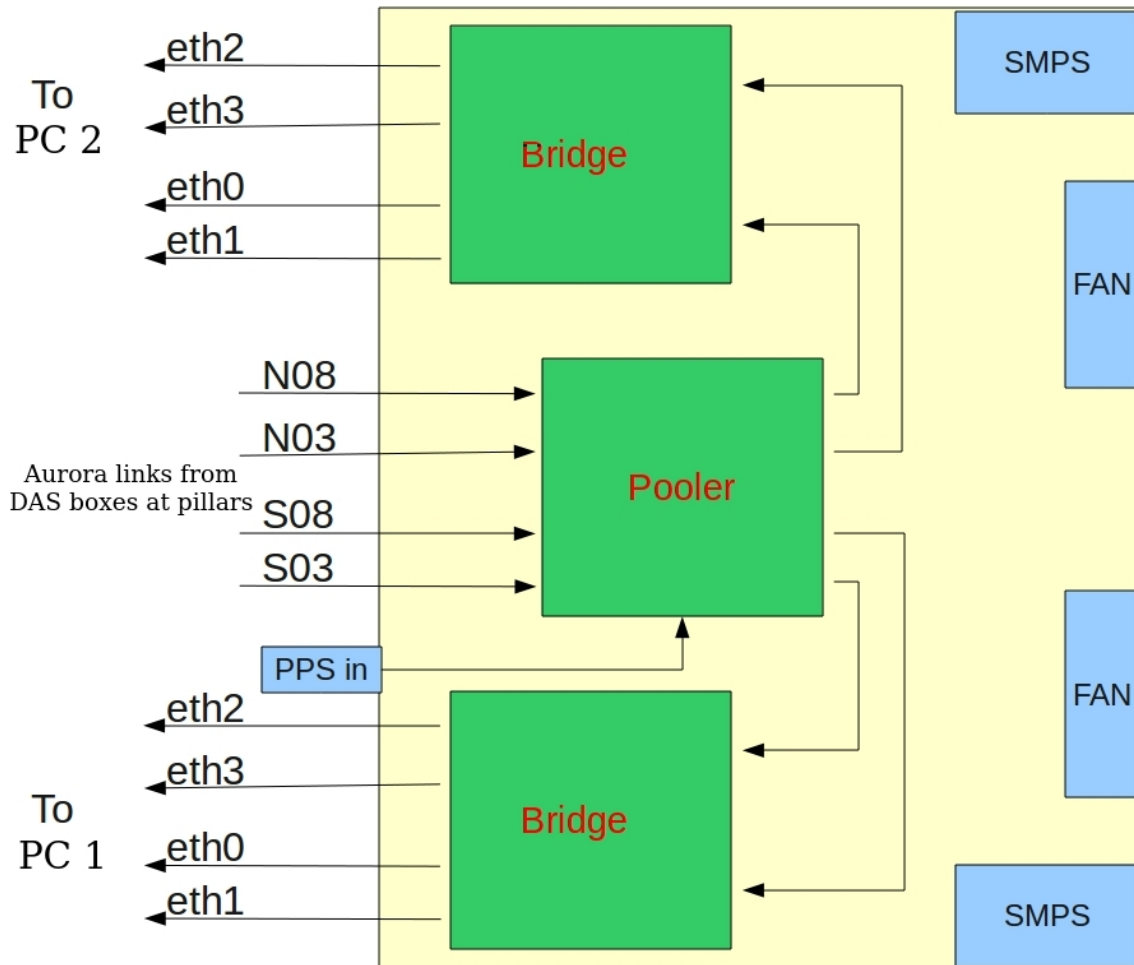
Figure 2.6.4: Data Acquisition system(at receiver room) for Phase **I**[27].

Gigabit Ethernet(GigE) links correspoding to one Aurora input. Hence, a bridge card takes two Aurora links as input and produces 4 GigE links as output.

The data is collected in distributed manner using two PCs. The GigE links from a bridge card are connected to the specific ports of a PC such that the MAC address of the links from FPGA side matches with the ones expected by the PC side. The GigE links from the bridge cards directly go into the PC ports not through a switch. Since, the two bridge cards have identical MAC/IP addresses which can clash if they are connected through a switch.

The Phase **I** DAS can operate in two modes, viz. Burst mode and continuous recording mode. In burst mode, it acquires all raw data from every pillar, with bursts

of 30 seconds where incoming data is stored continuously in PC RAM upto a prede-
fined limit and then slowly flushes to the disk. It can operate in continuous recording
mode but with lesser number of pillars.

In Phase **I**, Each antenna element is 11.5m along the length of the cylinder and 30m
wide. The smallest baseline corresponds to antenna separation of 11.5m and longest
baseline corresponds to 448.5m. The system has frequency bandwidth of 18 MHz.

2.6.2 Phase II

In Phase **II**, 4 successive dipoles are combined to form a single antenna element,
this gives rise to 264 antenna elements. Each element is amplified, filtered, directly
digitized in the field and is brought to the DAS system via fibre optic links.
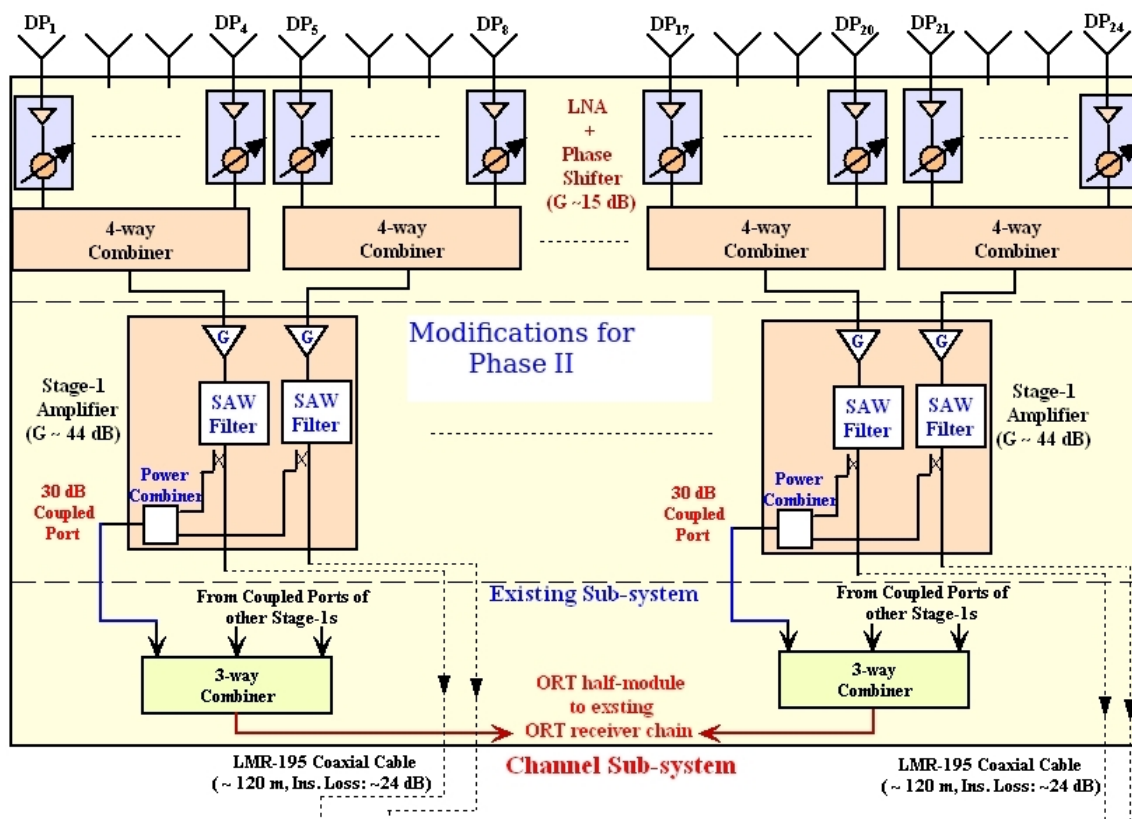
Figure 2.6.5: ORT sub-module for Phase **II**. The RF for the digital receiver is obtained
from the coupled ports[33].

In upgraded module for Phase **II** the 2-way combiners followed by the 4-way
combiners are replaced by stage-1 amplifiers. The stage-1 amplifiers(pre-amplifiers)

amplify the combined RF signal from 4-way combiners and feed it to the digital receiver. In addition, a coupled port is provided to interface the RF output to the existing analog system. This coupled port act as a 2-way combiner and the output is the combined signal of the two input signals, which is passed further to 3-way combiners in the analog sub-system. Figure 2.6.5 represents the upgraded sub-module for Phase **II**.

Data acquisition system for Phase II

The Signal from an antenna element(4 dioples combined) (see figure 2.6.5) is fed to a 12 channel Data Acquisition System(see fig.2.6.6). Digitized data from 264 antenna elements is transported to Pooler/Bridge systems using 44 fibre optic links in total(2-links per module). The final output is available in 8 independent sets of 11 Gigabit Ethernet links.
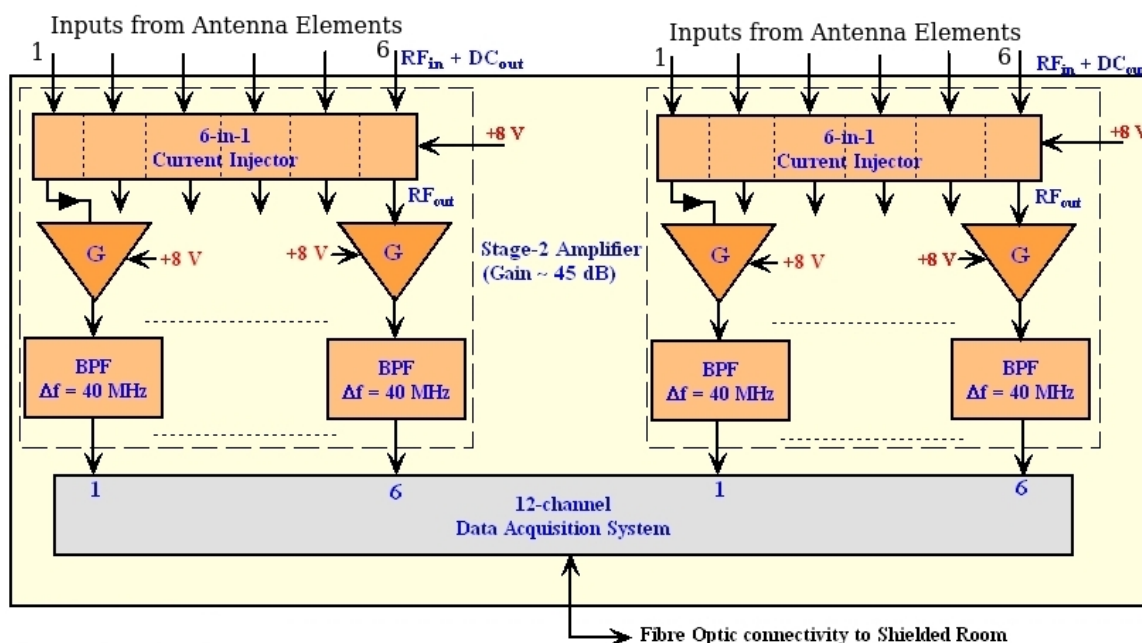
Figure 2.6.6: Data Acquisition sub-system(at Pillar) for Phase **II**[33].

Each fibre link carries data at 92.16 MB/s, therefore the total data output of the system is 8.11 GB/s. The Pooler/bridge system pools these data into 88 Gigabit ethernet ports connected to a unmanaged set of ethernet switches which are further linked to a High Performance Cluster (HPC).

Currently HPC used is a set of many-core processors with Intel's Sandy Bridge architecture. Each node will receive data from the bridge subsystem through a set

of 11 GigE links. Each node has a quad 8-core processor board with Intel Xeon Phi coprocessor. In a single node, the host processor interfaces with bridge cards through 11 GigE links, performs FFT and incorporates data partitioning & management functions, while the compute-intensive correlator is handled by the Xeon Phi coprocessor.

In Phase **II**, each antenna element is 1.92 m along the length of the cylinder and 30 m wide. The smallest baseline corresponds to the antenna separation of 1.9 m and longest baseline corresponds to 505.0 m. The system has frequency bandwidth of 30 MHz.

2.6.3 Performance of the Upgraded System

After Phase **I** upgrade, there will be 40 antenna elements and each antenna element will have rectangular aperture dimensions($b \times d$) equal to 30 m $\times$ 11.5 m. ORT will be able to provide instantaneous field of view of about 1.75° in E-W direction and 4.6° in N-S direction. The smallest baseline will correspond to antenna separation of 11.5 m and the largest baseline will correspond to 448.5 m. Total bandwidth of the system will be 18 MHz.The Phase **I** upgrade of ORT has completed and the system can be used for observations.

After Phase **II** upgrade, there will be 264 antenna elements and each antenna element will have rectangular aperture dimensions($b \times d$) equal to 30 m $\times$ 1.92 m. Telescope will be able to provide instantaneous field of view of about 1.75° in E-W direction and 27.4° in N-S direction with a resolution of 0.1°. This will provide an instantaneous coverage of about 3 steradians with an angular resolution of 1.75°$\times$ 0.1°. The smallest baseline will correspond to antenna separation of 1.9 m and the largest baseline will correspond to 505.0 m. Total bandwidth of the system will be 30 MHz. The phase **II** upgrade of ORT will be up and running by the end of 2014.

Table 2.1: System paramters for Phases **I** & **II** for upgraded ORT

Parameter	Phase **I**	Phase **II**
No. of antennas (N_A)	40	264
Aperture dimensions ($b \times d$)	30 m $\times$ 11.5 m	30 m $\times$ 11.5 m
Field of View(FoV)	1.75°$\times$ 4.6°	1.75°$\times$ 27.4°
Smallest baseline (d_{min})	11.5 m	1.9 m
Largest baseline (d_{max})	448.5 m	505.0 m
Angular Resolution	7'	6.3'
Total Bandwidth (B)	18 MHz	30 MHz
Single Visibility rms. noise (σ) assuming $T_{sys=}$ 150 K, $\eta = 0.6$, $\Delta\nu_c = 0.1$ MHz, $\Delta t = 16$ s	1.12 Jy	6.69 Jy
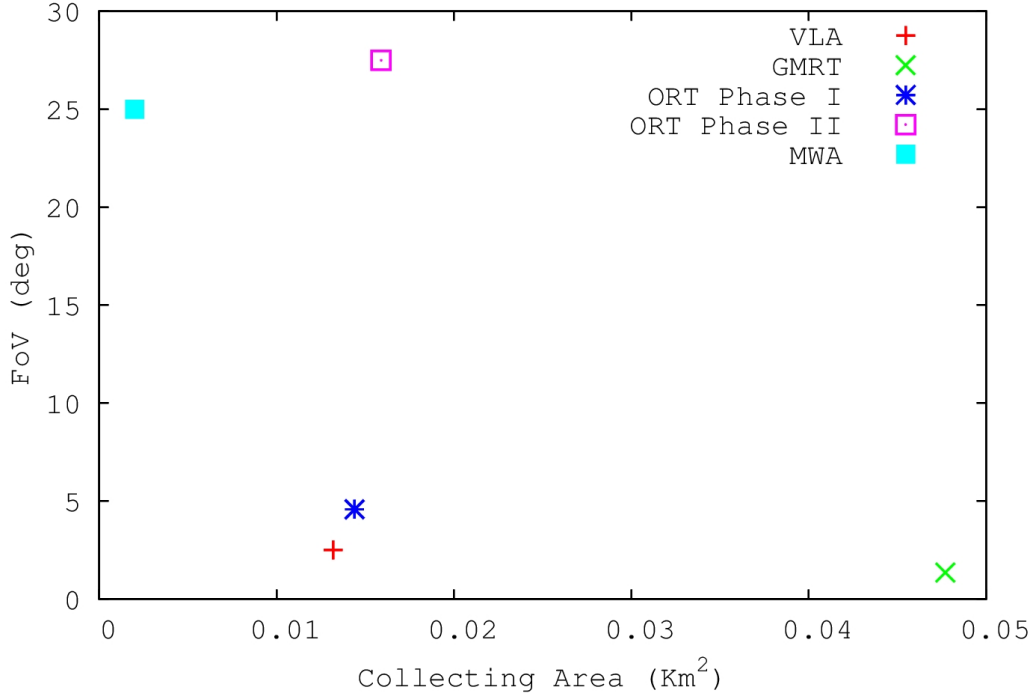
Figure 2.6.7: Comparison between different present interferomters indicated in the figure in terms of field of view and collecting area.

Figure 2.6.7 and 2.6.8 show a comparison between different present interferometers (VLA, GMRT, ORT and MWA) in terms of field of view & collecting area and frequeny bandwidth & collecting area respectively.
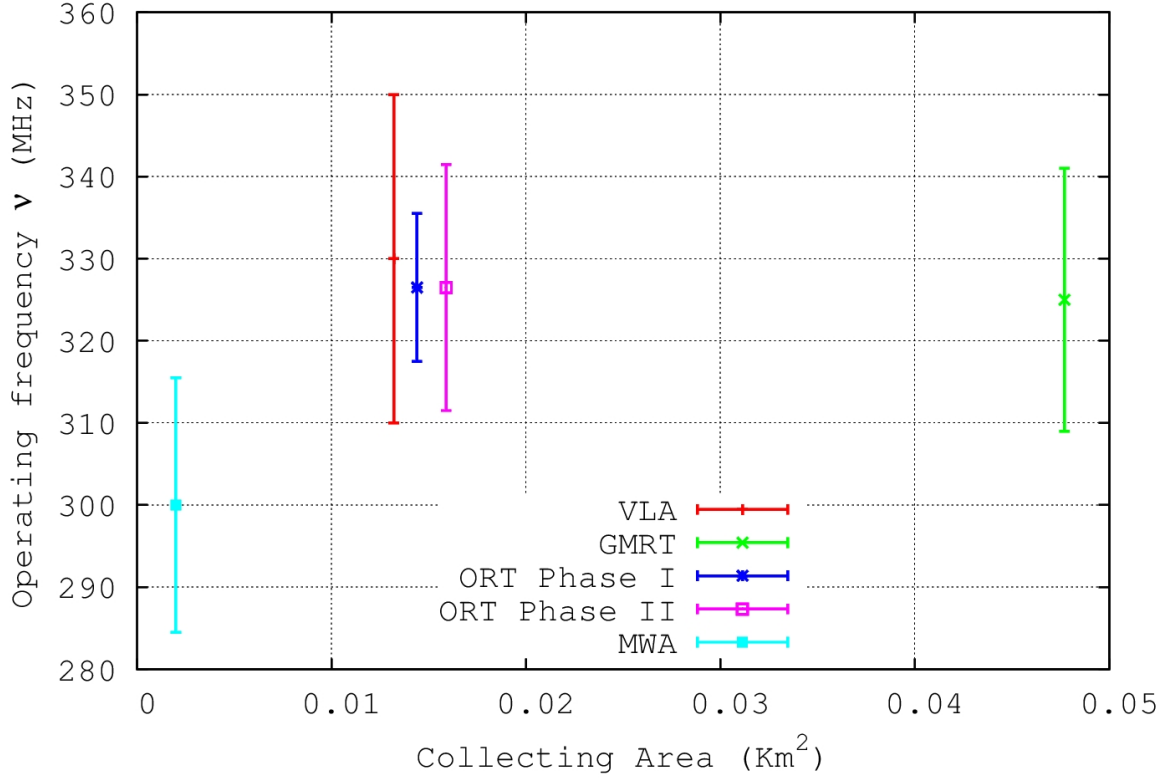
Figure 2.6.8: A comparison between different present interferometers indicated in the figure in terms of Operating frequency, Bandwidth and collecting area. The vertical lines represent the corresponding frequency bandwidth of the interferometers.

2.7 ORT Visibilities

The ORT antenna elements(after the upgradation) may be thought of as a linear array of N_A radio antennas, with each antenna located at a separation d along the length of the cylinder. When viewed from the direction of pointing of telescope, each antenna has rectangular aperture dimensions $b \times d$ where $b = 30$ m and $d = 11.5$ m & 1.9 m for Phase **I** & **II** respectively. Figure 2.7.1 represents tha antenna layout of ORT interferometer and aperture ($b \times d$) of antenna elements. The baselines are given by (Assuming that the aperture lie in $x - y$ plane with $x-$axis along the length of the cylinder),

$$U_1 = \left(\frac{d}{\lambda}\right)\hat{i}; \ U_1 = 2U_1; \ U_3 = 3U_1; \ ... \ U_{N_A-1} = (N_A - 1)U_1 \qquad (2.53)$$

The complex visibilities are recorded for these baselines. It can be seen that there is a huge redundancy(different antenna pairs correspond to same baseline) in the array due to its linearity and uniform spacing of the antenna elements. Any baseline U_n

46

occurs $M_n = (N_A - n)$ times in the array. The visibility $\mathcal{V}(U, \nu)$ for a given baseline U can be written as a fourier transform relationship (Van Cittert Zernike theorem in vector form) which is given by

$$\mathcal{V}(U, \nu) = \int d^2\vec{\theta}\ A(\vec{\theta}, \nu) I(\vec{\theta}, \nu) e^{-i2\pi U \cdot \vec{\theta}} \tag{2.54}$$

Where $A(\vec{\theta}, \nu)$ is the primary beam pattern or normalized power pattern (describes the response of an antenna towards the signals from different directions) of the individual antenna and $I(\vec{\theta}, \nu)$ is the specific intensity distribution on the sky. $\vec{\theta}$ is the 2-dimensional vector in the plane of sky $(l - m$ plane$)$ with origin at the center of the field of view.

Normalized power pattern $A(\vec{\theta}, \nu)$ of an antenna can be calculated by considering the antenna as an emitter instead of a receiver. It can be determined by calculating the normalized electric field pattern $E(\vec{\theta}, \nu)$ for far-field radiation. The normalized power pattern is given by $A(\vec{\theta}, \nu) = |E(\vec{\theta}, \nu)|^2$. $E(\vec{\theta}, \nu)$ can be determined by calculating the fourier transform of the electric field $\tilde{E}(U, \nu)$ at aperture. Since ORT responds only to a single polarization, therefore vector nature of the field $\tilde{E}(U, \nu)$ can be ignored. Also assuming that $\tilde{E}(U, \nu)$ is uniform everywhere on the aperture, $E(\vec{\theta}, \nu)$ is given by,

$$E(\vec{\theta}, \nu) = \operatorname{sinc}\left(\frac{\pi d\theta_x}{\lambda}\right) \operatorname{sinc}\left(\frac{\pi b\theta_y}{\lambda}\right) \tag{2.55}$$

therefore,

$$A(\vec{\theta}, \nu) = \operatorname{sinc}^2\left(\frac{\pi d\theta_x}{\lambda}\right) \operatorname{sinc}^2\left(\frac{\pi b\theta_y}{\lambda}\right) \tag{2.56}$$
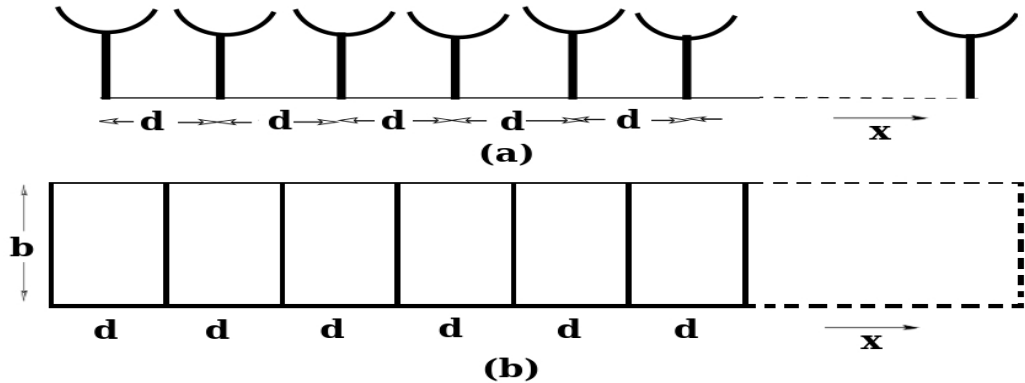

Figure 2.7.1: (a) Antenna layout when ORT is used as a radio-interferometer. (b) Aperture $(b \times d)$ of the individual antenna elements[8].

The actual beam pattern is expected to be somewhat broader than that predicted (Eq.2.56) if the dipole illumination pattern is also taken into account. The primary beam pattern decides the field of view of the interferometer. ORT has an asymmetric field of view i.e, beam has FWHM of $1.75°$ corresponding to b =30 m in the E-W direction and $4.6°$ & $27.4°$ in the N-S direction for Phase **I** & Phase **II** respectively.

The specific intensity can be decomposed into two terms viz. uniform background brightness and angular fluctuation in the specific intensity i.e,[8]

$$I(\vec{\theta}, \nu) = \bar{I}(\nu) + \delta I(\vec{\theta}, \nu) \tag{2.57}$$

Using this in Eq. 2.54 and experessing it as a convolution, we get

$$\mathcal{V}(U, \nu) = \tilde{A}(U, \nu)\bar{I}(\nu) + \tilde{A}(U, \nu) \otimes \Delta \tilde{I}(U, \nu) \tag{2.58}$$

Where $\tilde{A}(U, \nu)$ and $\Delta \tilde{I}(U, \nu)$ are fourier transforms of $A(\vec{\theta}, \nu)$ and $\delta I(\vec{\theta}, \nu)$ respectively. $\tilde{A}(U, \nu)$ is also referred as aperture power pattern & is given by the auto-convolution of the electric field at telescope aperture i.e, $\tilde{A}(U, \nu) = \tilde{E}(U, \nu) \otimes \tilde{E}(U, \nu)$, for a rectangular aperture

$$\tilde{A}(U, \nu) = \frac{\lambda^2}{bd} \Lambda\left(\frac{u\lambda}{d}\right) \Lambda\left(\frac{v\lambda}{b}\right) \tag{2.59}$$

where $\Lambda(x)$ is a triangular function defined as

$$\Lambda(x) = 1 - |x| \ \ \text{for} \ \ |x| < 1, \ \ \text{and} \ \ \Lambda(x) = 0 \ \ \text{for} \ \ |x| \geq 1. \tag{2.60}$$

It can be seen that the first term $\tilde{A}(U, \nu)\bar{I}(\nu)$ is resolved even before the smallest baseline U_1, therefore it is not necessary to consider the contribution from $\bar{I}(\nu)$ and can be ignored, so the Eq. 2.58 becomes

$$\mathcal{V}(U_n, \nu) = \int d^2 U' \tilde{A}(U_n - U', \nu) \Delta \tilde{I}(U', \nu) \tag{2.61}$$

Where each visibility $\mathcal{V}(U_n, \nu)$ is a weighted linear superposition of different fourier modes $\Delta \tilde{I}(U', \nu)$. I addition to sky signal each visibility also has a noise contribution $\mathcal{N}(U_n, \nu)$ i.e,

$$\mathcal{V}(U_n, \nu) = \mathcal{V}^{sky}(U_n, \nu) + \mathcal{N}(U_n, \nu) \tag{2.62}$$

Noise contribution $\mathcal{N}(U_n, \nu)$ is a Gaussian random field with zero mean and it is

independent of baselines i.e, each baseline will have different noise contribution. The real part of $\mathcal{N}(U_n, \nu)$ has *rms.* fluctuation σ given by[36]

$$\sigma = \frac{\sqrt{2}k_B T_{sys}}{\eta A \sqrt{\Delta\nu_c \Delta t}} \qquad (2.63)$$

Where T_{sys} is the total system temperature, k_B is the Boltzmann constant, $A = b \times d$ is the physical collecting area of each antenna, η is the aperture efficiency (accounts for the dipole illumination pattern upto some extent), $\Delta\nu$ is the channel width and Δt is the integration time. $T_{sys} \sim 150$ K for ORT, for observations with $\Delta\nu = 0.1$ MHz and $\Delta t = 16$s we have $\sigma = 1.12$ Jy for Phase **I** and 6.69 Jy for Phase **II** respectively.

The N-S axis of the cylindrical reflector of ORT is parallel to the Earth's rotation axis, and since all the baselines are alinged parallel to N-S axis of cylinder, the baselines too are parallel to the rotation axis of earth and do not change with the rotation of earth. For a particular baseline U_m, the visibility measured by any antenna pair (a, b) is product of the actual visibility $\mathcal{V}(U_m)$ and the unknown antenna gains g_a & g_b i.e, $\mathcal{V}'_{ab} = g_a g_b^* \mathcal{V}(U)$. As mentioned earlier, the array has considerable redundancy which means there are many antenna pairs which correspond to same actual visibility (since visibility depends on baselines only, not on antenna positions). Therefore, this redundancy can be used to recover true gains of the antennas and the true visibilities.

Chapter 3

Visibility correlations & HI power spectrum

3.1   Physics of 21cm HI line

The fundamental quantity of radiative transfer is the *brightness* (or specific intensity) I_ν of a ray emerging from a cloud at frequency ν. This conventionally expresses the energy carried by rays traveling along a given direction, per unit area, frequency, solid angle, and time.

I_ν can be quantified by the equivalent brightness temperature, $T_b(\nu)$, required of a blackbody radiator (with spectrum B_ν) such that $I_\nu = B_\nu(T_b)$. Throughout the range of frequencies and temperatures relevant to the 21 cm line, the Rayleigh-Jeans formula is an excellent approximation to the Planck curve (eq. 2.12), i.e. $T_b(\nu) = I_\nu c^2/2k_B\nu^2$, where is c is the speed of light and k_B is Boltzmann's constant.

We are interested in the brightness temperature of the 21 cm HI line ($\nu_\circ = 1420.4$ MHz). Because of the cosmological redshift, the emergent brightness $T_b^{'}(\nu)$ measured in a cloud's comoving frame at redshift z creates an apparent brightness at the Earth of $T_b(\nu) = T_b^{'}(\nu)/(1 + z)$, where the observed frequency is $\nu = \nu_\circ/(1 + z)$. Similarly, the brightness temperature of the CMB in a comoving frame at redshift z will be $T_\gamma^{'}(z) = 2.73(1 + z)K$.

An individual gas cloud produces a flux at the Earth of $S = \int_{cloud} d\Omega d\nu I_\nu cos\theta$, where the integral extends over the solid angle subtended by the cloud and the frequency spread of the signal. We will primarily be dealing with the frequency-dependent incident energy flux S_ν (measured in Janskys, $1Jy = 10^{-26}Wm^{-2}Hz^{-1}$). The apparent angle between center of the cloud and the solid angle is generally

small ($sin\theta \approx \theta$). Therefore, the flux-density can be described as $S_\nu = I_\nu \Delta\Omega = 2k_B T \nu^2 \Delta\Omega/c^2$, where all quantities are measured in observer's frame.

In the Rayleigh-Jeans limit, the equation of radiative transfer along a line of sight through a cloud of uniform excitation temperature T_{ex} states that the emergent brightness can be written as

$$T_b^{'}(\nu) = T_{ex}(1 - e^{-\tau_\nu}) + T_R^{'}(\nu)e^{-\tau_\nu} \tag{3.1}$$

where the *optical depth* $\tau_\nu \equiv \int ds\alpha_\nu$ is the integral of the absorption coefficient (α_ν) along the ray through the cloud, T_R is the brightness of the background radiation field incident on the cloud along the ray, and s is the proper distance.

For the 21 cm transition, the excitation temperature T_{ex} is referred to as the spin temperature T_S. It quantifies the relative number densities, n_i, of atoms in the two hyperfine levels of the electronic ground state. It is defined using

$$\frac{n_1}{n_0} = \frac{g_1}{g_0}e^{-E_{10}/k_B T_s} = 3e^{-T_\star/T_S} \tag{3.2}$$

Where subscripts 1 and 0 denote the triplet and singlet states respectively and $g_1 = 3$ & $g_0 = 1$ are the corresponding degeracies. $E_{10} = 5.9 \times 10^{-6}$ eV is the splitting energy and $T_\star = E_{10}/k_B = 0.068$ K is the equivalent temperature. Since $T_S \gg T_\star$, approximately 3 out of 4 atoms find themselves in excited state. As a result, the absorption coefficient must include a correction for stimulated emission and it depends on T_S as well. The optical depth of a Hydrogen cloud is then:

$$\begin{aligned}\tau_\nu &= \int ds\sigma_{01}(1 - e^{-E_{10}/k_B T_s})\phi(\nu)n_0 \\ &\approx \sigma_{01}\left(\frac{h\nu}{k_B T_s}\right)\left(\frac{N_{HI}}{4}\right)\phi(\nu)\end{aligned} \tag{3.3}$$

Where $\sigma_{01} \equiv \dfrac{3c^2 A_{10}}{8\pi\nu^2}$

$A_{10} = 2.85 \times 10^{-15}$ s^{-1} is the spontaneous emission coefficient of the 21 cm transition, N_{HI} is the column density of HI (the factor 1/4 accounts for the fraction of HI atoms in the hyperfine singlet state), $\phi(\nu)$ is the line profile ($\int \phi(\nu)d\nu = 1$). The equation(3.3) in approximate form assumes uniformity thoughout the cloud.

In general, the line shape $\phi(\nu)$ includes natural, thermal, and pressure broadening, as well as bulk motion (which increases the effective Doppler spread). Then the velocity broadening of a region of linear dimension s is $\Delta V \sim sH(z)$ so that $\phi(\nu) \sim c/[sH(z)\nu]$. The column density along such segment depends on the neutral fraction x_{HI} of Hydrogen, so $N_{HI} = x_{HI}n_H(z)s$. Therefore, expression for the optical depth of 21 cm Hydrogen (eq. 3.3) can be rewritten as:

$$
\begin{aligned}
\tau_\nu &= \frac{3}{32\pi}\frac{hc^3 A_{10}}{k_B T_S \nu_0^2}\frac{x_{HI}n_H}{(1+z)(dv_\parallel/dr_\parallel)} \\
&\approx (1+\delta)(1+z)^{3/2}\frac{x_{HI}}{T_S}\left[\frac{H(z)/(1+z)}{dv_\parallel/dr_\parallel}\right]
\end{aligned}
\tag{3.4}
$$

where T_S is in Kelvins, $(1+\delta)$ is the fractional overdensity of baryons and $dv_\parallel/dr_\parallel$ is the gradient of proper velocity along the line of sight (including Hubble expansion and peculiar velocity). $H(z)/(1+z)$ corresponds to the uniform Hubble expansion at higher redshifts. We are primarily interested in brightess temperature fluctuations (δT_b) between spin temperature(T_S) and CMB temperature (T_{CMB}) at high redshifts, which is given by

$$
\begin{aligned}
\delta T_b &= \frac{T_S - T_{CMB}(z)}{1+z}(1 - e^{-\tau_{\nu_0}}) \approx \frac{T_S - T_{CMB}(z)}{1+z}\tau_{\nu_0} \\
&\approx 9x_{HI}(1+\delta)(1+z)^{1/2}\left[1 - \frac{T_{CMB}}{T_S}\right]\left[\frac{H(z)/(1+z)}{dv_\parallel/dr_\parallel}\right] mK
\end{aligned}
\tag{3.5}
$$

Observations of 21 cm absorption by DLAS indicate that the spin temperature is orders of magnitude higher than the temperature of the cosmic microwave background radiation (CMBR) at the corresponding redshifts. This implies that the emission in the 21 cm hyperfine transition can be safely assumed to be proportional to the density of neutral Hydrogen[18].

3.2 HI Power Spectrum

It is known that the excess temperature observed at a frequency ν along a direction $\widehat{\mathbf{n}}$ is given by[16]

$$
T(\nu, \widehat{\mathbf{n}}) = \overline{T}(z)\eta_{HI}(z, \widehat{\mathbf{n}}r_\nu)
\tag{3.6}
$$

where $\nu = 1420/(1+z)$ is the frequency of observation and $r_\nu = \int_0^z \frac{c}{H(z')}dz'$ is the comoving distance and $\overline{T}(z)$ is given as

$$\overline{T}(z) = 4.0\text{mK}(1+z)^2 \left(\frac{\Omega_b h^2}{0.02}\right)\left(\frac{0.7}{h}\right)\left(\frac{H_0}{H(z)}\right) \tag{3.7}$$

The quantity $\eta_{HI}(z, \widehat{\mathbf{n}}r_\nu)$ is known as '21 cm radiation efficiency in redshift space' and can be written in terms of the mean neutral hydrogen fraction $\bar{x}_{HI}$ and the fluctuation in neutral hydrogen density field δ_{HI} as

$$\eta_{HI}(z, \widehat{\mathbf{n}}r_\nu) = \bar{x}_{HI}[1 + \delta_{HI}(z, \widehat{\mathbf{n}}r_\nu)]\left(1 - \frac{T_{CMB}}{T_S}\right)\left[1 - \frac{H(z)}{1+z}\frac{\partial v(z, \widehat{\mathbf{n}}r_\nu)}{\partial r_\nu}\right] \tag{3.8}$$

The term is square brackets arises from HI peculiar velocities. We have already assumed that $T_S \gg T_{CMB}$, we also assume that the HI peculiar velocity field is determined by the dark matter fluctuations since peculiar velocities mostly trace the dark matter potential wells. Therefore we can write

$$\eta_{HI}(z, \hat{\mathbf{n}}r_\nu) = \int \frac{d^3k}{(2\pi)^3}e^{ikr_\nu(\hat{\mathbf{k}}.\hat{\mathbf{n}})}\tilde{\eta}_{HI}(z, \mathbf{k}) \tag{3.9}$$

where

$$\tilde{\eta}_{HI}(z, \mathbf{k}) = \bar{x}_{HI}(z)[\Delta_{HI}(z, \mathbf{k}) + (\hat{\mathbf{k}}\cdot\hat{\mathbf{n}})^2\Delta(z, \mathbf{k})] \tag{3.10}$$

Where $\Delta_{HI}(z, \mathbf{k})$ and $\Delta(z, \mathbf{k})$ are the fourier transform of the fluctuations in the HI and the dark matter densities respectively. We use the multi-frequency angular power spectrum $C_l(\Delta\nu)$ to quantify the statistical properties of $\delta I(\overrightarrow{\theta}, \nu)$ (which refers to brightness temperature fluctuations $\delta T_b(\overrightarrow{\theta}, \nu)$).

Flat Sky Approximation

For the angular scales of our interest ($l \gg 1$), flat sky approximation can be used rather that using spherical harmonics to formulate $C_l(\Delta\nu)$. A small portion of the sky can be well approximated by a plane. The unit vector $\hat{\mathbf{n}}$ towards the direction of observation can be decomposed as

$$\hat{\mathbf{n}} = \mathbf{m} + \theta; \ \mathbf{m}\cdot\theta = 0; \ |\theta| \ll 1 \tag{3.11}$$

where $\mathbf{m}$ is a vector towards the center of the field of view and θ is a two-dimensional vector in the plane of the sky. Therefore, one can define the two-dimensional Fourier transform of $T(\nu, \hat{\mathbf{n}})$ in the flat-sky as

$$\tilde{T}(\nu, U) = \int d\theta e^{-i2\pi \mathbf{U} \cdot \theta} T(\nu, \hat{\mathbf{n}}) \tag{3.12}$$

where U corresponds to an inverse angular scale and is the Fourier conjugate of θ. Using flat sky approximation, we can write $\hat{\mathbf{k}} \cdot \hat{\mathbf{n}} \approx \hat{\mathbf{k}} \cdot \hat{\mathbf{m}} \equiv k_{\parallel}$, using this with equations (3.6) and (3.9) we get

$$\tilde{T}(\nu, U) = \frac{\bar{T}}{2\pi r_\nu^2} \int dk_{\parallel} e^{ik_{\parallel} r_\nu} \tilde{\eta}_{HI}(k_{\parallel}\hat{\mathbf{m}} + 2\pi \mathbf{U}/r_\nu) \tag{3.13}$$

$\tilde{\eta}_{HI}$ power spectrum P_{HI} can be defined as

$$\langle \tilde{\eta}_{HI}(\mathbf{k})\tilde{\eta}_{HI}(\mathbf{k}')\rangle = (2\pi)^3 \delta_D^3(\mathbf{k} - \mathbf{k}') P_{HI}(\mathbf{k}) \tag{3.14}$$

Assuming that HI traces the total matter distribution with a bias parameter, $P_{HI}(k, \mu) \equiv P_{HI}(\mathbf{k})$ can be modelled as

$$P_{\mathrm{HI}}(k, \mu) = b^2 \bar{x}_{\mathrm{HI}}^2 \left[1 + \beta\mu^2\right]^2 P(k) \tag{3.15}$$

where $\mu = \hat{\mathbf{k}} \cdot \hat{\mathbf{m}} = k_{\parallel}/k$ is the cosine of angle between $\mathbf{k}$ & line of sight and β is the linear distortion parameter. The μ dependence of $P_{HI}(\mathbf{k})$ arises from the peculiar velocities.

The correspondence between the all-sky angular power spectra and its flat-sky approximation is given by

$$\left\langle \tilde{T}(\nu_1, U)\tilde{T}^*(\nu_1, U')\right\rangle = C_{2\pi U}(\nu_1, \nu_2)\delta_D^{(2)}(\mathbf{U} - \mathbf{U}') \tag{3.16}$$

where $\delta_D^{(2)}$ is the 2-dimensional dirac delta function. Thus allows to estimate the angular power spectrum C_l under the flat-sky approximation which is given by:

$$C_l(\Delta\nu) = \frac{\bar{T}^2}{\pi r_\nu^2} \int_0^\infty dk_{\parallel} \cos(k_{\parallel} r_\nu' \Delta\nu) P_{\mathrm{HI}}(\mathbf{k}) \tag{3.17}$$

where $\mathbf{k}$ has magnitude $k = \sqrt{k_{\parallel}^2 + l^2/r_\nu^2}$ and has components $k_{\parallel}$ and l/r_ν along

the line of sight and in the plane of the sky respectively. Here r_ν is the comoving distance corresponding to $z = (1420\mathrm{MHz}/\nu) - 1$, $r'_\nu = \frac{dr_\nu}{d\nu}$. The flat sky approxmiation is not valid for the phase **II** of the upgraded ORT due to its large field of view.

We have used WMAP 9 power spectrum with ΛCDM cosmology for our calculations and the corresponding parameters are $H_0 = 70.0\mathrm{Km/s/Mpc}$, $\Omega_b h^2 = 0.02264$, $\Omega_\Lambda = 0.721, n_s = 0.972, \sigma_8 = 0.821$. Fig. 3.2.1 shows the WMAP 9 power spectrum for $z = 0$. We have used the value $x_{HI} = 2.45 \times 10^{-2}$ which corresponds to $\Omega_{gas} = 10^{-3}$[43].
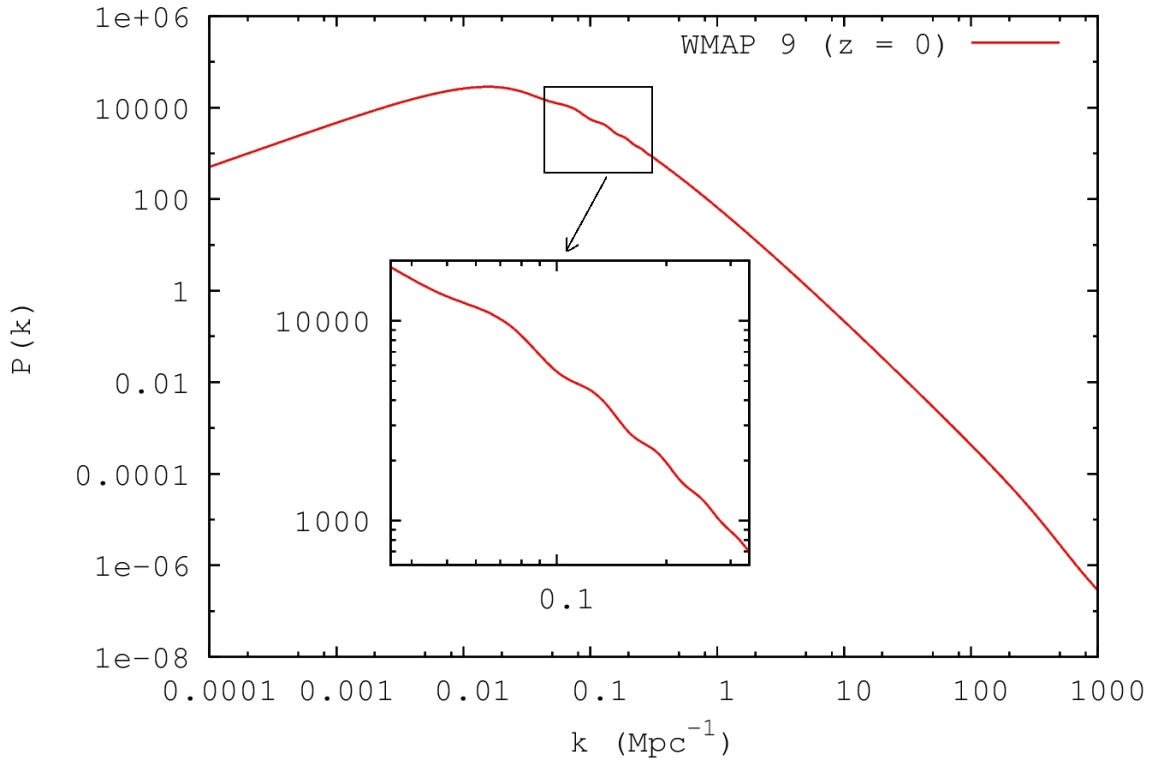

Figure 3.2.1: Shown is the linearly extrapolated matter power spectrum (z = 0), calculated using WMAP 9 cosmological parameters: $H_0 = 70.0\mathrm{Km/s/Mpc}$, $\Omega_b h^2 = 0.02264$, $\Omega_\Lambda = 0.721, n_s = 0.972, \sigma_8 = 0.821$. The inset shows BAO features.

We see that Phase **I** and Phase **II** are sensitive to $0.01 \leq k \leq 0.4\mathrm{Mpc}^{-1}$ and $0.002 \leq k \leq 0.5\mathrm{Mpc}^{-1}$ range respectively. We note that Phases **I** and **II** are both sensitive to the BAO feature which has the first peak at k = 0.045 Mpc−1 , and which has successive oscillations whose amplitude decays within $k = 0.3\mathrm{Mpc}^{-1}$ which is well within the k range that will be probed by ORT.

N-body simulations[2] (figure 3.2.2) indicate that it is reasonably well justified to assume a linear scale independent bias $b = 2$ for $k < 1\mathrm{Mpc}^{-1}$ with respect to the
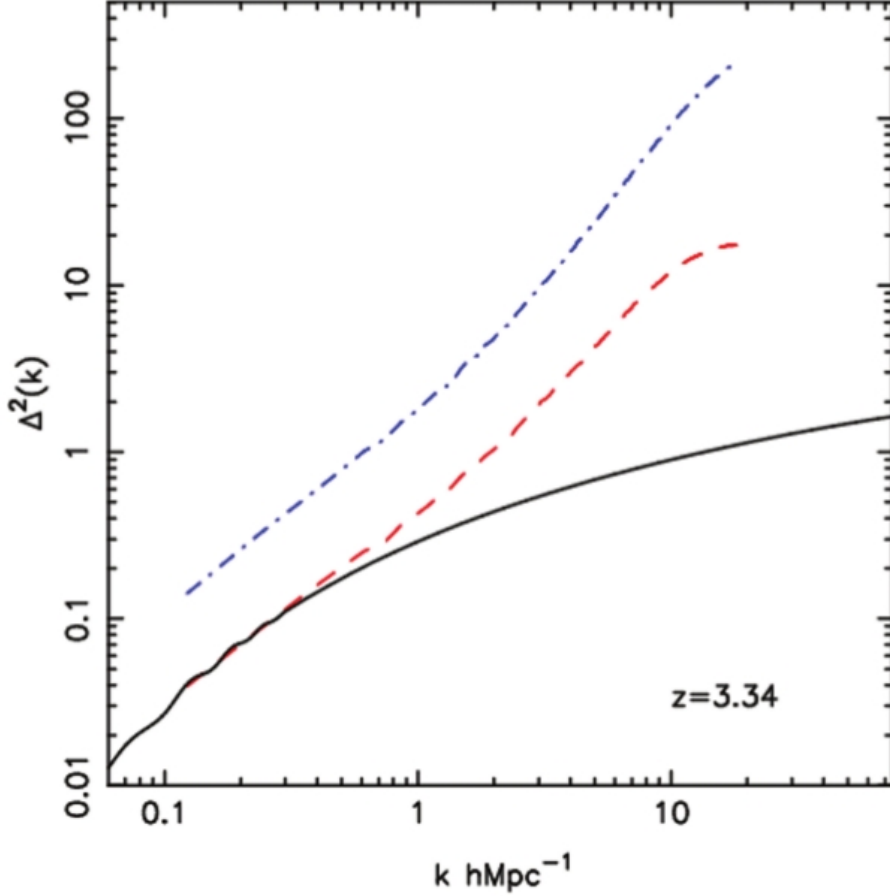
Figure 3.2.2: The power spectrum of fluctuations: the solid line shows the linearly extrapolated power spectrum, the dashed line shows the non-linear dark matter power spectrum and the dot–dashed line shows the HI power spectrum. All power spectra are for $z = 3.34$[2].

linear power spectrum. For $k > 1\mathrm{Mpc}^{-1}$, the bias b has a non-linear depenedence on k. We have modelled the non-linear dependence of bias $b \equiv b(k)$ in which $b(k)$ varies with k as

$$b(k) = \frac{b_0 + b_1(k/k_0)}{1 + b_2(k/k_1)} \tag{3.18}$$

where $b_0 = 2$, $b_1 = 1$, $b_2 = 1$, $k_0 = 1\mathrm{Mpc}^{-1}$ & $k_1 = 5\mathrm{Mpc}^{-1}$. We have employed both scale independent and scale dependent bias for our calculations of multi-frequency angular power spectrum $C_l(\Delta\nu)$ (fig. 3.2.3 and 3.2.4). These bias models still underestimates the power spectrum $P(k)$ at $k > 1\mathrm{Mpc}^{-1}$. Phase **I** and Phase **II** of upgraded ORT are sensitive to angular scales $75 \leq l \leq 3000$ and $13 \leq l \leq 3500$ respectively.
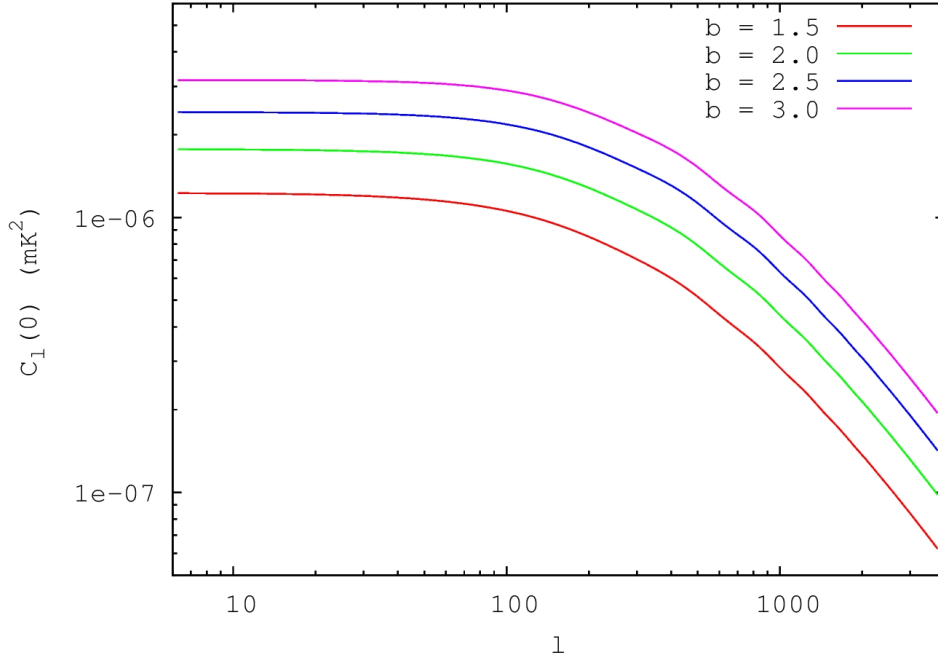
57

Figure 3.2.3: $C_l(0)$ as a function of l. The different curves correspond to different values of scale independent bias indicated in figure.
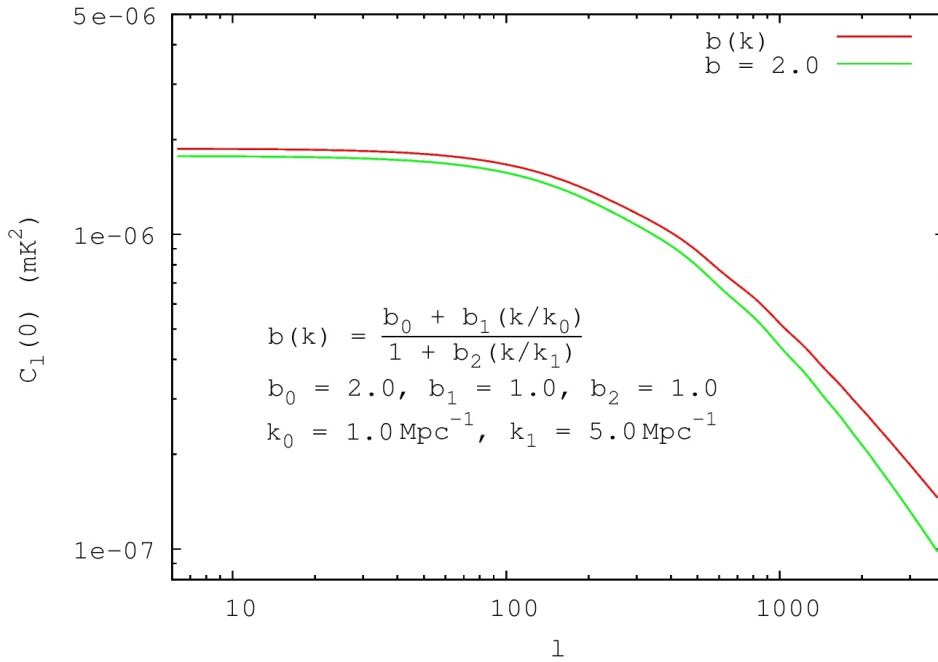

Figure 3.2.4: $C_l(0)$ as a function of l. The red curve corresponds to scale dependent bias (Eq.3.18) indicated in figure. The green curve corresponds to scale independent constant bias $b = 2.0$.

3.3   Visibility correlations

Visibility correlations can be used to describe the statistical properties of the angular and frequency domain fluctuations in the background radiation. We assume that the observed signal $\delta I(\vec{\theta}, \nu)$ is generated by a statistically homogeneous and isotropic random process (the process that generates $\delta I(\vec{\theta}, \nu)$ has no preferred origin or direction in sky and no preferred origin in frequency). We use the Multi-ferquency angular power spectrum $C_l(\delta\nu)$ in flat sky approximation can be used to describe the properties of $\delta I(\vec{\theta}, \nu)$.

The 2-D power spectrum (flat-sky approximation) is defined using

$$\langle \Delta\tilde{I}(U, \nu)\Delta\tilde{I}^*(U', \nu + \Delta\nu)\rangle = P(U, \Delta\nu)\delta_D^2(U - U') \qquad (3.19)$$

Where $\delta_D^2(U - U')$ is the 2-D Dirac delta function. $C_l(\delta\nu)$ refers to $\delta T(\vec{\theta}, \nu)$ which is the brightness temperature corresponding to $\delta I(\vec{\theta}, \nu)$. Therefore,

$$C_l(\Delta\nu) = \left(\frac{\partial B}{\partial T}\right)^{-2} P(l/2\pi, \Delta\nu) \qquad (3.20)$$

Where l corresponds to 2D wave vector $2\pi U$ with $l = 2\pi|U|$, and B is the Planck function. $C_l(\delta\nu)$ defined above characterizes both angular (l) and frequency dependence ($\Delta\nu$) of the sky signal. The visibilities $\mathcal{V}(U_n, \nu)$ are related to $C_l(\delta\nu)$ through visibility correlations, which can be written as (combining Eq. 2.61, 3.19 & 3.20)

$$\langle \mathcal{V}(U_n, \nu)\mathcal{V}^*(U_m, \nu + \Delta\nu)\rangle = \left(\frac{\partial B}{\partial T}\right)^2 \int d^2U' \tilde{A}(U_n - U', \nu) \times$$
$$\tilde{A}^*(U_m - U', \nu + \Delta\nu)C_{2\pi U'}(\Delta\nu) \qquad (3.21)$$

The functions $\tilde{A}(U_n - U', \nu)$ and $\tilde{A}^*(U_m - U', \nu + \Delta\nu)$ overlap only when $|n-m| \leq 1$. This implies that the two visibilities are correlated only if they correspond to same baselines or nearest neighbours. In case of same baselines and ignoring the slow $\Delta\nu$ dependence of $\tilde{A}^*(U_m - U', \nu + \Delta\nu)$, the two visibility correlation can be expressed as

$$V_2(U_n, \Delta\nu) \equiv \langle \mathcal{V}(U_n, \nu)\mathcal{V}^*(U_m, \nu + \Delta\nu)\rangle \qquad (3.22)$$

Therefore,

$$V_2(U_n, \Delta\nu) = \left(\frac{\partial B}{\partial T}\right)^2 \int d^2U' |\tilde{A}(U_n - U', \nu)|^2 C_{2\pi U'}(\Delta\nu) \qquad (3.23)$$

For large baselines, above equation can be approximated as

$$V_2(U_n, \Delta\nu) = \left(\frac{\partial B}{\partial T}\right)^2 \left[\int d^2U' |\tilde{A}(U_n - U', \nu)|^2\right] C_l(\Delta\nu) \qquad (3.24)$$

Which can be simplified to

$$C_l(\Delta\nu) = 0.26 \left(\frac{\text{mK}}{\text{Jy}}\right)^2 \left(\frac{bd}{m^2}\right) V_2(U_n, \Delta\nu) \qquad (3.25)$$

$V_2(U_n, \Delta\nu)$ can be determined directly from the measured visibilities and hence $C_l(\Delta\nu)$, which describes the statistical properties of brightness temperature distribution on the sky. The above equation provides a reasonably good approximation for nearly entire basline range covered by ORT.

We now discuss the $\Delta\nu$ dependence of the signal $S_2(U, \Delta\nu)$. We use decorrelation function $\kappa_U(\Delta\nu)$[16] to quantify this $\Delta\nu$ dependence. $\kappa_U(\Delta\nu)$ can be defined as

$$\kappa_U(\Delta\nu) = \frac{S_2(U, \Delta\nu)}{S_2(U, 0)} \qquad (3.26)$$

This function quantifies how quickly the HI signal decorrelates as the frequency separation $\Delta\nu$ increases. The signal is perfectly correlated at $\Delta\nu = 0$ where we have $\kappa_U(0) = 1$, and the correlation falls ($\kappa_U(\Delta\nu) < 1$) as $\Delta\nu$ is increased.

Figure 3.3.1 shows $\kappa_U(\Delta\nu)$ as a function of $\Delta\nu$ for different baselines **U**. The predictions are the same for Phase **I** and **II**. We see that $\kappa_U(\Delta\nu)$ varies slowly with $\Delta\nu$ at the small baselines. For **U** = 10, we have $\kappa_U(\Delta\nu) = 0.5$ at $\Delta\nu \approx 1\text{MHz}$, beyond which κ falls further. The value of κ_U crosses zero at around $\Delta\nu \approx 4\text{MHz}$, and becomes negative beyond this. At larger baselines, $\kappa_U(\Delta\nu)$ has a steeper depenedence with $\Delta\nu$. For **U** = 200, we see that $\kappa_U(\Delta\nu) = 0.5$ at $\Delta\nu \approx 0.2\text{MHz}$, and κ_U crosses zero at around $\Delta\nu \approx 1\text{MHz}$. We also see that values of κ_U oscillate around zero at high $\Delta\nu$ values. We have defined $\Delta\nu_{0.9}$, $\Delta\nu_{0.5}$ and $\Delta\nu_{0.1}$ as the values of the frequency separation $\Delta\nu$ where the decorrelation falls to 0.9, 0.5 and 0.1 respectively i.e. $\kappa_U(\Delta\nu_{0.5}) = 0.5$, etc. Figure 3.3.2 shows $\Delta\nu_{0.9}$, $\Delta\nu_{0.5}$ and $\Delta\nu_{0.1}$ as a function of **U**.
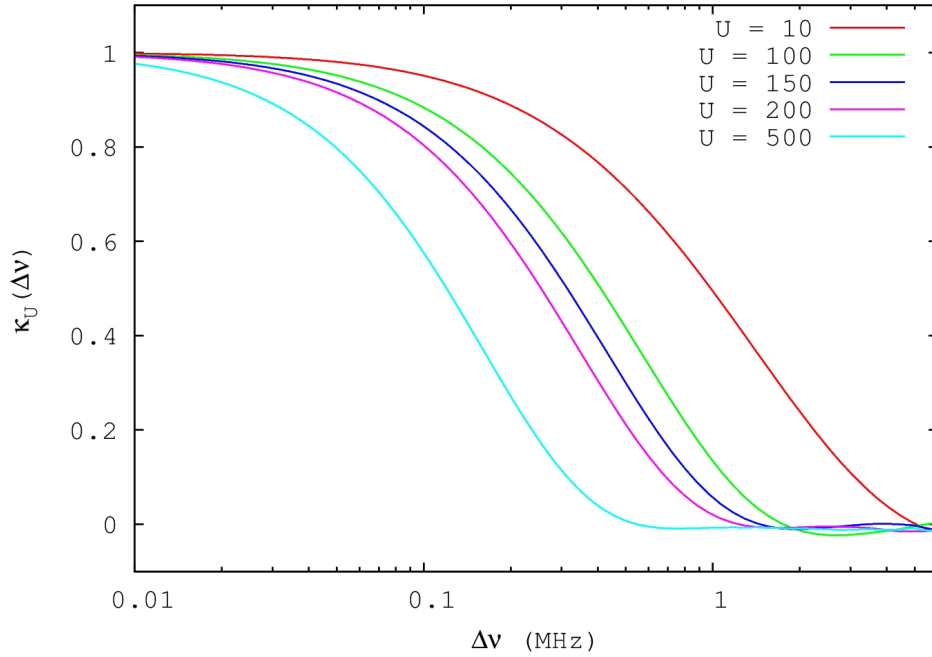
Figure 3.3.1: Frequency decorrelation function $\kappa_U(\Delta\nu)$ as a function of $\Delta\nu$ at five different **U** values indicated in figure. The signal decorrelates more sharply for higher value of **U**.

Figure 3.3.2: This figure shows how $\Delta\nu$ is varying as a function of **U** for a given values of frequency decorrelation function $\kappa_U(\Delta\nu)$ indicated in the figure.

We observe that, BAO features are clearly visible in $(\Delta\nu, U)$ space on the contour of $\kappa_U(\Delta\nu) = 0.1$. The oscillations are also present in $\kappa_U(\Delta\nu) = 0.5$ but have a smaller amplitude.

Chapter 4

Prospects of HI detection using Upgraded ORT

Simulated maps of HI distribution in the post-reionization era are generally used to study the prospects for detection with 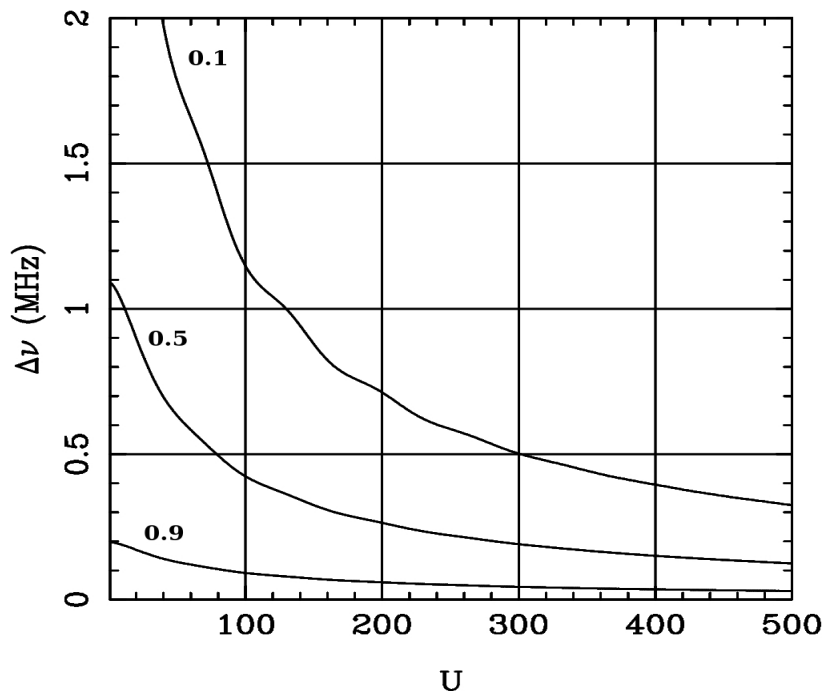existing and upcoming radio telescopes. We consider detection in the redshifted radiation from the hyperfine transition with a rest frame frequency of 1420 MHz. Possibility of a statistical detection using visibility correlations is discussed. We show that the upgraded ORT can potentially detect signal from the HI distribution at high redshifts and compare the same with the present and upcoming instruments like GMRT(Giant Meterwave Radio Telescope), MWA(Murchinson Widefield Array), SKA(Square Kilometre Array) etc.

We have used the WMAP 9 power spectrum for the matter distribution at $z = 3.35$ (assuming that HI traces the total matter power spectrum) to compute visibility correlations using the formulation discussed in chapter 3. We estimate the noise level for upgraded ORT and compare it with the expected signal.

4.1 Noise in Visibility Correlations

The contribution to the measured visibilities $\mathcal{V}(U_n, \nu)$ from the sky signal (Eq. 2.61) is a combination of three different components

$$\mathcal{V}(U_n, \nu) = \mathcal{S}(U_n, \nu) + \mathcal{N}(U_n, \nu) + \mathcal{F}(U_n, \nu) \tag{4.1}$$

where $\mathcal{S}(U_n, \nu)$ is the HI signal which is the object of our study here, $\mathcal{F}(U_n, \nu)$ is the contribution from other astrophysical sources referred to as the foregrounds

and $\mathcal{N}(U_n, \nu)$ is the system noise contribution. We treat all of these as uncorrelated random variables with zero mean. Therefore, we can write the visibility correlation equation

$$V_2(U_n, \Delta\nu) = S_2(U_n, \Delta\nu) + N_2(U_n, \Delta\nu) + F_2(U_n, \Delta\nu) \qquad (4.2)$$

where S_2, F_2 and N_2 respectively are the signal, foreground and the noise contribution to the visibility correlation.

Radiation from different astrophysical sources other than the cosmological HI signal collectively known as foregrounds. Foregrounds include extragalactic point sources, diffuse synchrotron radiation from our Galaxy & low redshift galaxy clusters; free-free emission from our Galaxy (GFF) & external galaxies (EGFF). Extra-galactic point sources and the diffuse synchrotron radiation from our Galaxy dominate the foreground radiation at 326.5 MHz. The contribution of free-free emissions from our Galaxy and external galaxies is very small compared to the above but each of these is individually larger than the HI signal. All these foregrounds are continuum sources and the frequency dependence of these various continuum foreground components can be modelled by power laws. Refer [29][32][15][21][5] for a detailed discussion on foregrounds.

The baseline range $U \leq 10$ of ORT is dominated by the synchrotron radiation, whereas $10 \leq U \leq 300$ is dominated by the clustering of the point sources and $U \geq 300$ is dominated by the Poisson contribution. The contributions from the Galactic and extra-galactic free-free emission are considerably smaller across the entire U range. The total foreground contribution to each visibiity is around $104 - 105$ times larger than the HI signal. In our calculations we have assumed that all foreground are already removed from the signal (zero foreground contribution) and treated the total signal consisting of only HI signal and noise.

The real part of $\mathcal{N}(U_n, \nu)$ has rms. fluctuation σ given by (Eq. 2.63)

$$\sigma = \frac{\sqrt{2}k_B T_{sys}}{\eta A \sqrt{\Delta\nu_c \Delta t}} \qquad (4.3)$$

The noise in the visibilities measured at different antenna pairs is uncorrelated. As mentioned earlier, the ORT has a high degree of redundancy and there are many independent antenna pairs corresponding to the same baseline. Further, an observation spanning a total observing time of t_{obs} provides $t_{obs}/\Delta t$ different measurements of each visibility. The noise in the visibilities measured at two different time instants is uncorrelated. It is possible to avoid the noise contribution $N_2(U_n, \Delta\nu)$ in the visibility

correlation $V_2(U_n, \Delta\nu)$ by correlating only the visibility measurements where the noise is uncorrelated. For a fixed baseline $\mathbf{U}$ we only correlate the visibilities measured by different antenna pairs or the visibilities measured at different time instants.

The total error in the residual visibility correlation has two parts arising from the cosmic variance and the system noise respectively. The expected uncertainty or statistical fluctuations in the visibility correlation is

$$\sqrt{(\Delta V_2)^2} = \sqrt{(\Delta S_2)^2 + (\Delta N_2)^2} \tag{4.4}$$

where $(\Delta S_2)^2$ and $(\Delta N_2)^2$ are the cosmic variance and system noise contributions respectively.

We have $(\Delta N_2)^2 = (2\sigma^2)^2$ and $(\Delta S_2)^2 = (S_2)^2$ for a single estimate of the visibility correlation. The system noise contribution reduces to $(\Delta N_2)^2 = (2\sigma^2 \Delta t/t_{obs})^2$ if we combine the measurements at different time instants. Moreover, the redundant baselines provide many estimates of the visibility correlation (ΔV_2) at the same $\mathbf{U}$ where each estimate has an independent system noise contribution, but signal however is the the same. We have also bin the data by combining the estimates of $V_2(U_n, \Delta\nu)$ at the different $\mathbf{U}$ values within a finite bin width of our choice. The different baselines $\mathbf{U}$ provide independent estimates of both the signal and the system noise.

The frequency bandwidth B also provides several independent estimates of the visibility correlation. The value of $\Delta\nu_{0.5}$ (corresponding to $\kappa_U(\Delta\nu) = 0.5$)provides an estimate of the frequency separation over which the HI signal remains correlated. We also assume that the frequency bandwidth B provides us with $B/(\Delta\nu_{0.5})$ independent estimates of the visibility correlation. Combining all the effects discussed above we have

$$(\Delta N_2)^2 = \left(\frac{2\sigma^2 \Delta t}{t_{obs}}\right)^2 \frac{\Delta\nu_{0.5}}{N_P B} \text{ and } (\Delta S_2)^2 = \frac{(S_2)^2 \Delta\nu_{0.5}}{N_E B} \tag{4.5}$$

We have binned the data into logarithmic basline bins and N_P and N_E denote the number of independent estimates of the system noise and the signal in $V_2(U_n, \Delta\nu)$ respectively for each bin.

The system noise contribution (ΔN_2) dominates over the cosmic variance (ΔS_2) in entire baseline range, i.e. (ΔN_2) has major contribution in the total uncertainty (ΔV_2). We observe that 1σ detection is possible with 10^3 hrs of integration for the signal with scale independent bias binned with 9 logarithmic bins on baseline scale for the baseline range of $\mathbf{U} \sim 30 - 150$ (fig. 4.1.1). 2σ detection is possible for the
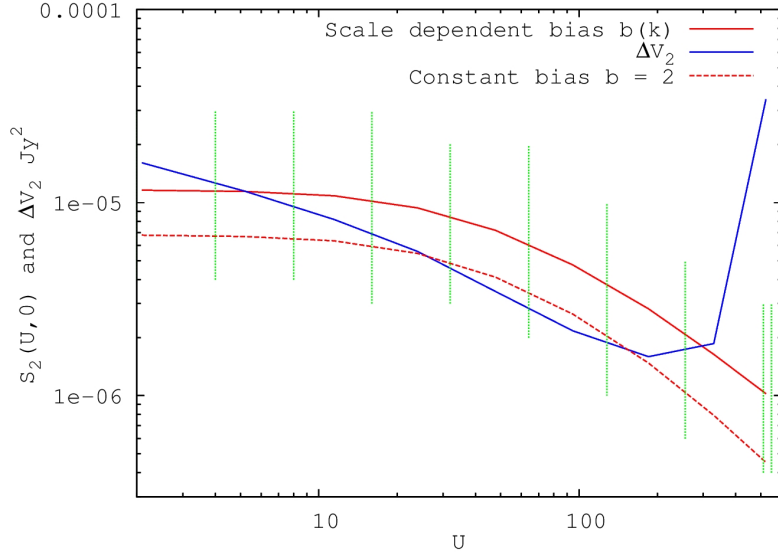
Figure 4.1.1: Shown is the expected signal and system noise as a function of **U** for the Phase **II** of upgraded ORT. The red curves show the expected HI signal $S_2(U_n, \Delta\nu)$ for $\Delta\nu = 0$ for two different bias models, dashed curve shows the expected signal with scale independent bias $b = 2.0$ and solid curve shows the expected signal with scale dependent bias $b(k)$ (eq. 3.18). while the blue curve shows the 1σ errors for the observation time indicated in the figure. The data is binned with 9 logarithmic bins, the green vertical lines show the starting and ending positions of the bins.

signal with scale dependent bias $b(k)$ (eq. 3.18), with 10^3 hrs of integration for the baseline range of **U** $\sim 30 - 150$ (fig 4.1.1).

We have done a similar analysis to calculate expected signal and noise but with the bin size used is double the bin size used for figure 4.1.1. We observe that optimizing the bin size gives better detection possibility. We see that detection with significance greater than 1.5σ is possible with 10^3 hrs of integration for the signal with scale independent bias binned with 5 logarithmic bins on baseline scale for the baseline range of **U** $\sim 20 - 200$ (fig. 4.1.2). 3σ detection is possible for the signal with scale dependent bias $b(k)$ (eq. 3.18), with 10^3 hrs of integration for the baseline range of **U** $\sim 10 - 200$ (fig 4.1.2).

We have compared our results for upgraded ORT with the calculations done by Bagla et al(2010)[2] for GMRT and MWA. Figure 4.1.3 and 4.1.4 show the expected signal and system noise calculated for GMRT and MWA respectively. We observe that HI detection not possible with either GMRT or MWA for 10^3 hrs of integration time. This make upgraded ORT a potential candidate for HI signal detection from post-reionization era at redshift $z = 3.35$.
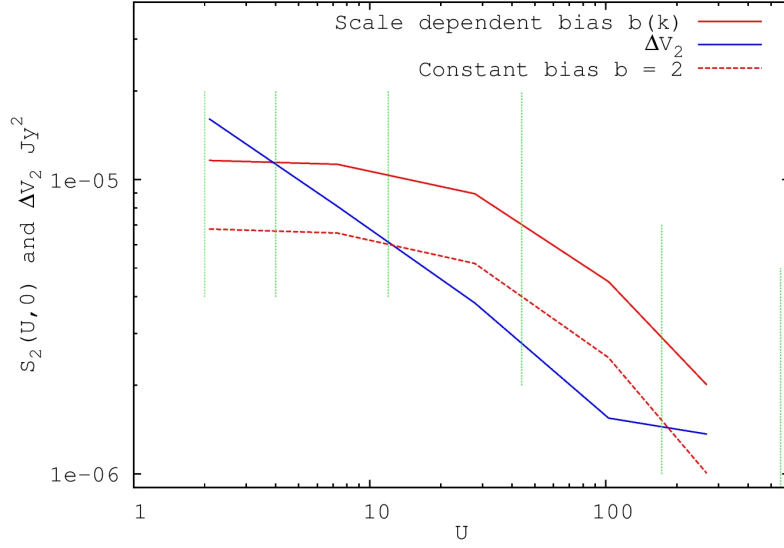
Figure 4.1.2: Shown is the expected signal and system noise as a function of **U** for the Phase **II** of upgraded ORT. The red curves show the expected HI signal $S_2(U_n, \Delta\nu)$ for $\Delta\nu = 0$ for two different bias models, dashed curve shows the expected signal with scale independent bias $b = 2.0$ and solid curve shows the expected signal with scale dependent bias $b(k)$ (eq. 3.18). while the blue curve shows the 1σ errors for the observation time indicated in the figure. The data is binned with 5 logarithmic bins. The green vertical lines show the starting and ending positions of the bins.
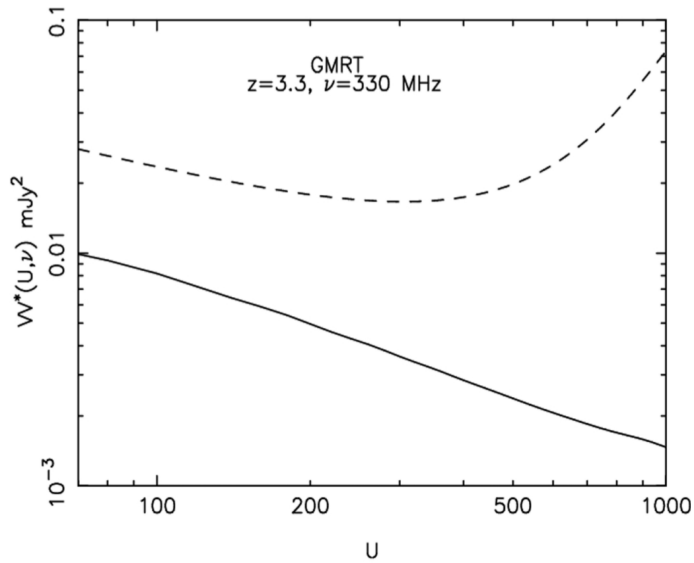

Figure 4.1.3: Shown is the expected signal(visibility correlation) as a function of U for GMRT computed for 10^3 hrs of integration. The expected signal is shown with a solid curve and the expected noise in the visibility correlation is shown by a dashed curve[2].

67

Figure 4.1.4: Shown is the expected signal(visibility correlation) as a function of U for MWA with 10^3 hrs of integration. The expected signal is shown with a solid curve and the expected noise in the visibility correlation is shown by a dashed curve[2].
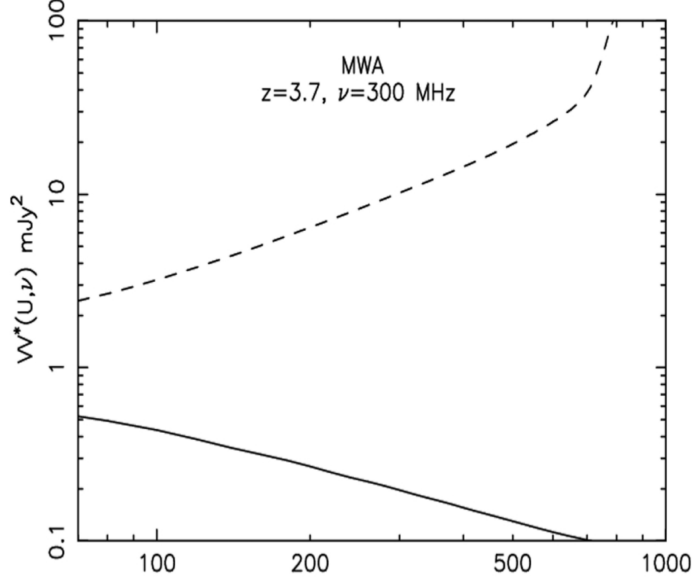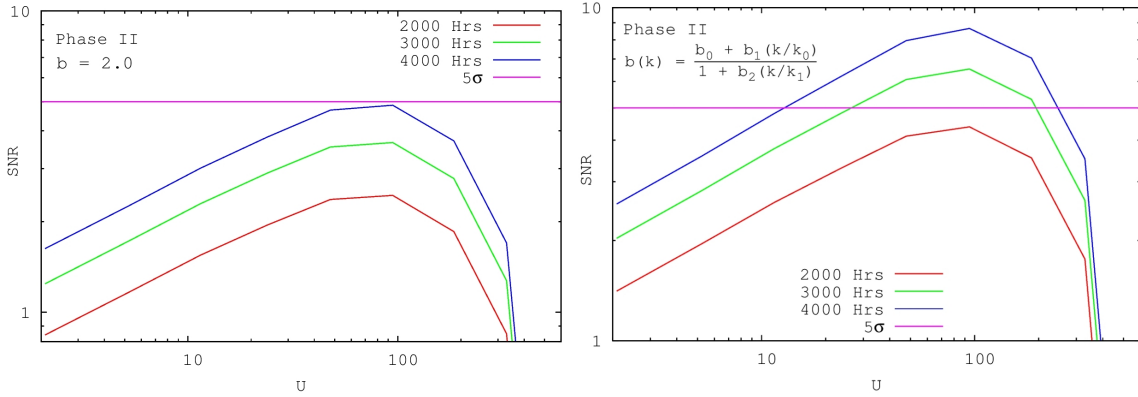

Figure 4.1.5: This figure shows the signal to noise ratio (SNR) as function of baseline **U** with data divided in 9 logarithmic bins for different integration times indicated. Left panel shows SNR calcuated for the signal with scale independent bias $b = 2.0$. Right panel shows SNR calcuated for the signal with scale dependent bias $b(k)$(eq. 3.18). The horizontal line corresponds to SNR = 5.

We have investigated the SNR for detecting the HI signal under the assumption that it is possible to completely remove the foregrounds. Figure 4.1.5 shows the Signal to Noise ratio as a function of baselines with data binned in 9 logarithmic bins. The SNR shown in figure 4.1.5 peaks around **U** ~ 100. We see that 3σ detection of the signal with scale independent bias is possible in the baseline range $40 \leq$ **U** ≤ 100

with ~ 3000 hrs of integration with the (fig. 4.1.5 left panel). Whereas 5σ detection is possible for the signal with scale dependent bias in baseline range $30 \leq \mathbf{U} \leq 200$ with ~ 3000 hrs of integration (fig. 4.1.5 right panel).
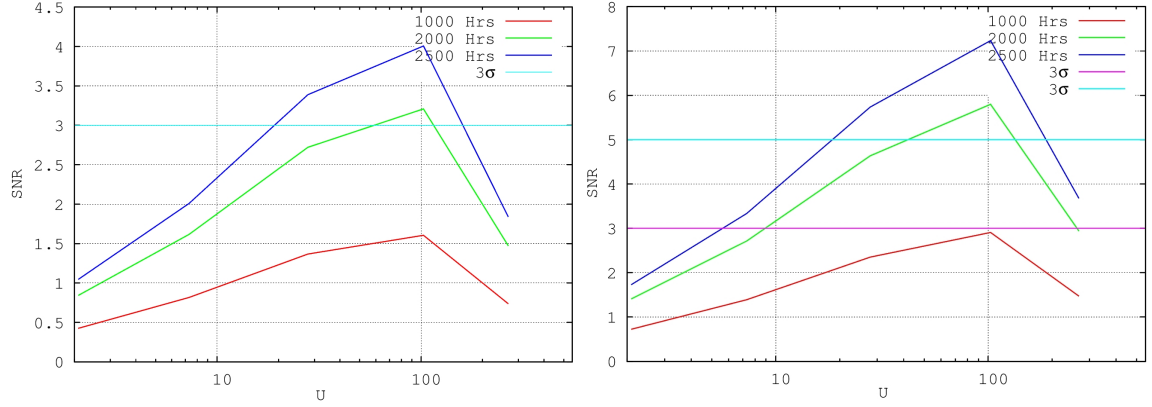

Figure 4.1.6: This figure shows the signal to noise ratio (SNR) as function of baseline **U** with data divided in 9 logarithmic bins for different integration times indicated. Left panel shows SNR calcuated for the signal with scale independent bias $b = 2.0$. Right panel shows SNR calcuated for the signal with scale dependent bias $b(k)$(eq. 3.18). The horizontal lines corresponds to SNR = 3 and 5 as indicated in figure.

We have performed a similar SNR calculation but with data divided in 5 logarithmic bins (double the bin size in previous calculation). We observe that optimizing bin size leads to a detection with better significance level. We see that for the bin size mentioned above, a 3σ detection of the signal with scale independent bias is possible in ~ 2000 hrs of integration (fig. 4.1.6 left panel). Whereas $> 2\sigma$ detection is possible for the signal with scale dependent bias in baseline range with ~ 1000 hrs of integration and 5σ detection with ~ 2000 hrs of integration(fig. 4.1.6 right panel).

BAO features in the expected signal have much smaller amplitude compared to the signal, therefore to make a BAO detection huge integration times and multiple realizations will be required.

The HI detection prospects with upgraded ORT are very promising. Optimizing the bin sizes, the realizations can lead to detections with higher significance level in smaller integration times. From the comparison of HI detection prospects with ORT, GMRT and MWA we conclude that at present ORT is the only instrument which can detect HI signal at z 3.35 with 10^3 hrs of integration. Except the upgraded ORT, only SKA-mid has the potential to detect HI signal at this particular redshift in smaller

integration times. Construction of SKA-mid will finish around year 2022. It is expected that more than a calender year will be required to make a good HI detection with upgraded ORT, this 8 year window till the completion of SKA-mid provides an opportunity to make a significant detection with phase **II** of upgraded ORT. There is another upgrade planned for ORT which will increase the redshift range probed by ORT from $z = 3.35$ to $z = 1 - 5$. After this upgrade ORT will be able to probe almost full range of post-reionzation era. This upgrade will also come up before the completion of SKA-mid construction and will provide opportunity to make a detection in the redshift range mentioned above.

Bibliography

[1] Anish Roshi et al., *A survey of recombination line emission from the Galactic plane at 325 MHz.*, Astrophys Astr, vol 6, p 171 (1985)

[2] Bagla, J. S., Khandai, N., Datta, K. K., *HI as a probe of the large-scale structure in the post-reionization universe.*, MNRAS, 931 (2010)

[3] Bagla J. S., Nath B., Padmanabhan T., *Neutral hydrogen at high redshifts as a probe of structure formation-III. Radio maps from N-body simulations.*, MNRAS, 289, 671 (1997)

[4] Becker R. H., et al., *Evidence for Reionization at z 6: Detection of a Gunn-Peterson Trough in a z=6.28 Quasar.*, AJ, 122, 2850 (2001)

[5] Bernardi G., et al., *Foregrounds for observations of the cosmological 21 cm line. I. First Westerbork measurements of Galactic emission at 150 MHz in a low latitude field*, A & A, 500, 965 (2009)

[6] Bharadwaj S., Ali S. S., *The CMBR fluctuations from HI perturbations prior to reionization.*, MNRAS, 352, 142 (2004)

[7] Bharadwaj S., Ali S. S., *On using visibility correlations to probe the HI distribution from the dark ages to the present epoch - I. Formalism and the expected signal.*, MNRAS, 356, 1519 (2005)

[8] Bharadwaj S., Ali S. S., *Prospects for detection of redshifted 21cm HI signal at 325 MHz with ORT* arXiv:1310.1707v2 (2014)

[9] Bharadwaj S., Nath B., Sethi S.K. *Using HI to probe large scale structures at $z \sim 3$.*, JApA. 22, 21 (2001)

[10] Bharadwaj S., Sethi S. K., *HI Fluctuations at Large Redshifts: I-Visibility correlation.*, JApA, 22, 293 (2001)

[11] Bharadwaj S., Sethi S., Saini T. D., *Estimation of cosmological parameters from neutral hydrogen observations of the post-reionization epoch.*, Phys Rev. D, 79, 083538 (2009)

[12] Binney J., *The physics of dissipational galaxy formation.*, ApJ, 215, 483 (1977)

[13] Chang et al., *Baryon Acoustic Oscillation Intensity Mapping as a Test of Dark Energy.*, Phys Rev. Lett., 100, 091303 (2008)

[14] Chengalur et al., *Low frequency radio astronomy.* (2003)

[15] Cress C. M., Helfand D. J., Becker R. H., Gregg M. D., White R. L., *Probing density fluctuations using the FIRST radio survey.*, Ap.J, 473, 7 (1996)

[16] Datta K. K., Roy Choudhury, T., Bharadwaj. S., *The multifrequency angular power spectrum of the epoch of reionization 21-cm signal* , MNRAS, 378, 119 (2007)

[17] Fan X., Carilli C. L., Keating B., *Observational Constraints on Cosmic Reionization.*, ARA& A, 44, 415 (2006)

[18] Furlanetto, S. R., Oh, S. P., Briggs, F. H., *Cosmology at Low Frequencies: The 21 cm Transition and the High-Redshift Universe.*, PHYS REP, 433, 181 (2006)

[19] Kapahi V. K., Damle S. H., Balasubramanian V., Swarup G., *An Electrically Steerable Array of 968 Dipoles for the Ooty Radio Telescope.*, J. Instn Electronics & Telecom. Engrs., Vol. 25, No. 3, (1975)

[20] Komatsu E., et al., *Five year Wilkinson Microwave Anisotropy Probe observations: Cosmological interpretation.* , ApJS, 180, 330 (2009)

[21] La Porta L., Burigana C., Reich W. et al., *The impact of Galactic synchrotron emission on CMB anisotropy measurements.*, A & A, 479, 641 (2008)

[22] Loeb A., Zaldarriaga M., *Measuring the Small-Scale Power Spectrum of Cosmic Density Fluctuations through 21 cm Tomography Prior to the Epoch of Structure Formation.*, Phys. Rev. Lett., 92, 211301 (2004)

[23] Manoharan P. K., Ananthakrishnan S., *Determination of solar-wind velocities using single-station measurements of interplanetary scintillation.*, MNRAS, vol 244, p 691-695 (1990)

[24] McKee C. F., Ostriker E. C., *Theory of Star Formation.*, ARA& A, 45, 565 (2007)

[25] Mould J. R., et al., *Combining the Constraints on the Hubble Constant.*, ApJ, 529, 786 (2000)

[26] Peebles P. J. E., *Principles of physical cosmology.*, Princeton University Press (1993).

[27] Peeyush Prasad, *A Network Centric Receiver Architecture for Low Frequency Arrays.*, PhD Thesis, Raman Research Inst, Bangalore, India (2011)

[28] Rees M. J., Ostriker J. P., *Cooling, dynamics and fragmentation of massive gas clouds - Clues to the masses and radii of galaxies and clusters.*, MNRAS, 179, 541 (1977)

[29] Santos, M.G., Cooray, A.,Knox, L., *Multifrequency Analysis of 21 cm Fluctuations from the Era of Reionization.*, Ap.J, 625, 575 (2005)

[30] Sarma N.V.G., Joshi M.N., Bagri D.S., Ananthakrishnan S., *Receiver System of the Ooty Radio Telescope.*, J. Instn Electronics & Telecom. Engrs., Vol. 21, No. 3, (1975)

[31] Selvanayagam A.J., Praveenkumar A., Nandagopal D.,Velusamy T., *Sensitivity Boost to the Ooty Radio Telescope: A New Phased Array of 1056 Dipoles with 1056 Low Noise Amplifers.*, IETE Technical review Vol 10, No.4, (1993)

[32] Singal J., Stawarz L., Lawrence A., Petrosian V., *Sources of the radio background considered.*, MNRAS, 409, 1172 (2010)

[33] Subrahmanya C.R., *ORT as a 264-Element Synthesis Telescope.*, March, 2013.

[34] Subrahmanyan R., *Observational constraints on the formation of pregalactic condensates in the universe.*, PhD Thesis, Indian Inst Sci, Bangalore, India (1989)

[35] Swarup G. et al., *Large Steerable Radio Telescope at Ootacamund, India.*, Nature Physical Science, Vol. 230, Apr, (1971)

[36] Thompson, A.R., Moran, J.M., Swenson, G.W., *Interferometry and Synthesis in Radio Astronomy*, John Wiley & Sons, pp. 160 (1986)

[37] Uson J. M., Bagri D. S., Cornwell T. J., *Radio detection of neutral Hydrogen at redshift $z = 3.4$.*, Phys Rev Lett, vol 67, pp 3328-3331 (1991)

[38] Visbal, E., Loeb, A., Wyithe, S., *Cosmological Constraints from 21cm Surveys After Reionization.*, JCAP, 10, 30 (2009)

[39] Weinberg S., *Cosmology*, Oxford University Press (2008)

[40] Wolfe A. M., Gawiser E., Prochaska J. X., *Damped Ly α Systems.*, ARA& A, 43, 861 (2005)

[41] Wyithe, S., Loeb, A., *The 21cm Power Spectrum After Reionization.*, arXiv:0808.2323 (2008)

[42] Wyithe, S., Loeb, A., Geil, P., *Baryonic Acoustic Oscillations in 21cm Emission: A Probe of Dark Energy out to High Redshifts.*, arXiv:0709.2955 (2007)

[43] Zafar, T., P roux, C., Popping, A., et al., *The ESO UVES Advanced Data Products Quasar Sample - II. Cosmological Evolution of the Neutral Gas Mass Density.*, AAP, 556, A141 (2013)

[44] Zinnecker H., Yorke H. W., *Toward Understanding Massive Star Formation.*, ARA& A, 45, 481 (2007)

[45] http://www.hartrao.ac.za/synthesis_school/Miod_Array_Design.pdf